

UPDATED 34-BAND PHOTOMETRY FOR THE SINGS/KINGFISH SAMPLES OF NEARBY GALAXIES

D. A. DALE¹, D. O. COOK², H. ROUSSEL³, J. A. TURNER¹, L. ARMUS⁴, A. D. BOLATTO⁵, M. BOQUEN⁶, M. J. I. BROWN⁷, D. CALZETTI⁸, I. DE LOOZE⁹, M. GALAMETZ^{10,11}, K. D. GORDON¹², B. A. GROVES¹³, T. H. JARRETT¹⁴, G. HELOU⁴, R. HERRERA-CAMUS¹⁵, J. L. HINZ¹⁶, L. K. HUNT¹⁷, R. C. KENNICUTT¹⁸, E. J. MURPHY¹⁹, A. REST¹², K. M. SANDSTROM²⁰, J.-D. T. SMITH²¹, F. S. TABATABAEI²², C. D. WILSON²³

¹Department of Physics & Astronomy, University of Wyoming, Laramie WY, USA; ddale@uwyo.edu

²Cahill Center for Astronomy & Astrophysics, California Institute of Technology, Pasadena CA, USA

³Institut d'Astrophysique de Paris, Sorbonne Universités, Paris, France

⁴Spitzer Science Center, California Institute of Technology, Pasadena, CA, USA

⁵Department of Astronomy, University of Maryland, College Park, MD, USA

⁶Unidad de Astronomía, Universidad de Antofagasta, Antofagasta, Chile

⁷School of Physics & Astronomy, Monash University, Victoria 3800, Australia

⁸Department of Astronomy, University of Massachusetts, Amherst MA, USA

⁹Sterrenkundig Observatorium, Universiteit Gent, Gent, Belgium

¹⁰European Southern Observatory, Garching, Germany

¹¹Laboratoire AIM, CEA, Université Paris Diderot, IRFU/Service d'Astrophysique, Gif-sur-Yvette, France

¹²Space Telescope Science Institute, Baltimore MD, USA

¹³Research School of Astronomy & Astrophysics, Australian National University, Canberra, Australia

¹⁴Astronomy Department, University of Capetown, Rondebosch, South Africa

¹⁵Max-Planck-Institut für Extraterrestrische Physik, Garching, Germany

¹⁶Steward Observatory, University of Arizona, Tucson AZ, USA

¹⁷INAF - Osservatorio Astrofisico di Arcetri, Firenze, Italy

¹⁸Institute of Astronomy, University of Cambridge, Cambridge, UK

¹⁹National Radio Astronomy Observatory, Charlottesville, VA, USA

²⁰Center for Astrophysics and Space Science, University of California, San Diego CA, USA

²¹Department of Physics & Astronomy, University of Toledo, Toledo, OH, USA

²²Instituto de Astrofísica de Canarias, La Laguna, Spain

²³Department of Physics & Astronomy, McMaster University, Hamilton, Ontario, Canada

ABSTRACT

We present an update to the ultraviolet-to-radio database of global broadband photometry for the 79 nearby galaxies that comprise the union of the KINGFISH (Key Insights on Nearby Galaxies: A Far-Infrared Survey with *Herschel*) and SINGS (*Spitzer* Infrared Nearby Galaxies Survey) samples. The 34-band dataset presented here includes contributions from observational work carried out with a variety of facilities including *GALEX*, *SDSS*, *Pan-STARRS1*, *NOAO*, *2MASS*, *WISE*, *Spitzer*, *Herschel*, *Planck*, *JCMT*, and the *VLA*. Improvements of note include recalibrations of previously-published SINGS $BVR_{\text{C}}I_{\text{C}}$ and KINGFISH far-infrared/submillimeter photometry. Similar to previous results in the literature, an excess of submillimeter emission above model predictions is seen primarily for low-metallicity dwarf/irregular galaxies. This 33-band photometric dataset for the combined KINGFISH+SINGS sample serves as an important multi-wavelength reference for the variety of galaxies observed at low redshift. A thorough analysis of the observed spectral energy distributions is carried out in a companion paper.

Keywords: ISM: general — galaxies: ISM — infrared: ISM

1. INTRODUCTION

Access to panchromatic broadband photometry for galaxies is crucial to fully understanding the characteristics of, and relative contributions to, galaxy spectra from the various processes related to interstellar attenuation, star formation,

and the feeding of supermassive black holes (Silva et al. 1998; da Cunha et al. 2008; Boquien et al. 2016). Though a fairly complete multi-wavelength dataset has been published for the SINGS (*Spitzer* Infrared Nearby Galaxies Survey) sample of 75 nearby galaxies (Kennicutt et al. 2003; Dale et al. 2005, 2007), subsequent far-infrared/submillimeter *Herschel* broadband data were later published for the KINGFISH (Key Insights on Nearby Galaxies: A Far-Infrared Survey with *Herschel*) sample of 61 nearby galaxies (Kennicutt et al. 2011; Dale et al. 2012), a sample for which 57 of the 61 targets are also SINGS targets. The photometric datasets from the combined SINGS/KINGFISH surveys have served as important references for studies seeking to understand the diverse properties of galaxies in the Local Universe (da Cunha et al. 2008; Noll et al. 2009; Jonsson et al. 2010; Rémy-Ruyer et al. 2015), or to serve as redshift-zero comparison samples to higher redshift galaxies (Kartaltepe et al. 2010; Maiolino et al. 2015; Scoville et al. 2016).

In this effort we present an update to the global (spatially-integrated) photometry for the 79 nearby galaxies that comprise the union of the KINGFISH and SINGS samples. This update includes a recalibration of the Dale et al. (2012) KINGFISH far-infrared/submillimeter photometry, necessary since the calibration of the *Herschel* photometers has undergone multiple revisions since those data were first published. We also carry out a *Pan-STARRS1*-based recalibration of the $BVR_C I_C$ fluxes previously published in Dale et al. (2007). A portion of those ground-based broadband optical data is suspect, since the data were originally taken in non-photometric conditions, and the ensuing attempts to calibrate the non-photometric frames were insufficient. We also include new $ugriz$ and 12 μm photometry, respectively from the *Sloan Digital Sky Survey* (*SDSS*) and the *Wide-Field Infrared Survey Explorer* (*WISE*) mission. In addition, the *Herschel* PACS photometry for KINGFISH galaxy NGC 0584 was not included in Dale et al. (2012) since those imaging data were not yet taken. Furthermore, we include new *Herschel* photometry for six SINGS galaxies from the *Herschel* Very Nearby Galaxy Survey (PI C. Wilson) that are not in the KINGFISH sample (NGC 2403, M81=NGC 3031, M82=NGC 3034, NGC 4125, M51a=NGC 5194, and M51b=NGC 5195). Finally, we complete the presentation of a multi-wavelength database by including previously published global photometry from ultraviolet (*GALEX*), infrared/submillimeter (*2MASS*, *Spitzer*, SCUBA), and radio (*VLA*) wavelengths.

Section 2 provides a brief overview of the galaxy sample, Section 3 recaps the relevant observations and approaches to data processing, Section 4 describes the salient results, and Section 5 provides the summary. The companion paper (Hunt et al. 2017) explores the observed spectral energy distributions (SEDs) by utilizing and comparing fits using three popular fitting tools: GRASIL, MAGPHYS, and CIGALE (Silva et al. 1998; da Cunha et al. 2008; Noll et al. 2009).

2. GALAXY SAMPLE

Table 1 presents the full list of 79 galaxies that form the union of the SINGS and KINGFISH samples. The sample was chosen to be a representative sampling of the Local Universe; the sample is not volume-limited and thus does not represent a statistical sampling of the Local Volume, but the sample is representative of the diversity of local galaxies. These galaxies were selected to span a range of morphologies, colors, and luminosities (e.g., Figures 5 and 3, respectively, of Kennicutt et al. 2003; Dale et al. 2012). Figure 1 demonstrates the sample’s range of optical colors and near-infrared luminosities; a few galaxies reside in the red sequence near the top of the diagram but most of the sample spans the blue star-forming sequence. The sample is comprised of 8%, 11%, 63%, and 18% early-type, lenticular, spiral, and irregular galaxies, respectively, based on the optical morphologies provided in the NASA/IPAC Extragalactic Database (NED). This galaxy sample has no sources for which the optical luminosity is dominated by AGN emission, though one-third have signatures of Seyfert/LINER nuclei (Tajer et al. 2005; Dale et al. 2006; Moustakas et al. 2010; Grier et al. 2011). There are only a few galaxies that are undoubtedly interacting with neighboring galaxies including NGC 5194 (with NGC 5195), NGC 1097 (with NGC 1097A), NGC 1316 (with NGC 1317), and NGC 3190 (with NGC 3187). The distances reach out to ~ 30 Mpc with a median value of ~ 10 Mpc.

3. OBSERVATIONS AND DATA PROCESSING

Much of the photometry presented here has already been described in Dale et al. (2007) and Dale et al. (2012), so we focus the following discussion on important differences from what is presented in those publications. The imaging bandpasses utilized here are listed in the heading of Table 2. The central wavelengths and widths of the filters are computed via

$$\bar{\lambda} \equiv \frac{\int \lambda \mathcal{T}(\lambda) d\lambda}{\int \mathcal{T}(\lambda) d\lambda} \quad (1)$$

$$\Delta \equiv \int \mathcal{T}(\lambda) d\lambda \quad (2)$$

where \mathcal{T} represents the filter transmittance normalized to peak at unity, based on the filter profiles compiled by Noll et al. (2009) for use in the CIGALE software package (Noll et al. 2009).

3.1. Ground-based Optical

Some of the optical $BVR_{\text{C}}I_{\text{C}}$ photometry from Dale et al. (2007) suffer from faulty calibration (Muñoz-Mateos et al. 2009). Sometimes insufficient numbers of standard star observations were taken; sometimes the standards were saturated; and some of the frames taken in non-photometric conditions were not successfully calibrated *a posteriori*. A recalibration is carried out here via comparison of photometry on foreground stars in *Pan-STARRS1* (PS1) $g_{\text{PS1}}r_{\text{PS1}}i_{\text{PS1}}z_{\text{PS1}}$ and in our 2007-era $BVR_{\text{C}}I_{\text{C}}$ imaging. The PS1 3π Survey utilizes the 1.8 m telescope on Mount Haleakala to map the sky north of $\delta = -30^{\circ}$ with multiple passes of 30–60 sec exposures in each of their five *SDSS*-like filters (Schlafly et al. 2012; Magnier et al. 2013).

Care was taken in the comparison to only use bright ($r_{\text{PS1}} < 19$ mag), unsaturated sources with point spread functions (PSFs) that agree with the seeing profiles of each image (i.e., background galaxies are excluded). The median number of foreground stars per galaxy utilized for this purpose was 15. Aperture diameters for the foreground stellar photometry were typically 7"; increasing the aperture diameter by 50% results in a <1% difference in the calibration. The PS1 fluxes were converted from their measured values at 1.2 airmasses to 0 airmasses (Table 4 of Tonry et al. 2012), and the small (tens of millimag) corrections suggested by Scolnic et al. (2015) were incorporated (see their Table 3); the small calibration modifications of Scolnic et al. (2015) are based on a “super calibration” that combines flux measurements of secondary standards from several surveys including PS1 and *SDSS*.

We adopted the Tonry et al. (2012) quadratic filter transformations for stars between *Pan-STARRS1* $g_{\text{PS1}}r_{\text{PS1}}i_{\text{PS1}}z_{\text{PS1}}$ and $BVR_{\text{C}}I_{\text{C}}$, though very similar results are obtained when using linear transformations between *SDSS* and Johnson/Cousins filters (Jester et al. 2005; Lupton et al. 2005; Chonis & Gaskell 2008; Jordi et al. 2006; Tonry et al. 2012). The only significant outliers for any of these various stellar transformations are the Chonis & Gaskell (2008) V and Lupton et al. (2005) R_{C} linear transformations, both of which yield calibrations that ultimately result in galaxy fluxes that are 25–30% ($\sim 0.25 - 0.30$ mag) brighter compared to when using other published transformations. The photometric calibrations are derived in practice from the error-weighted differences between the instrumental $BVR_{\text{C}}I_{\text{C}}$ fluxes and the measured PS1 fluxes (transformed to $BVR_{\text{C}}I_{\text{C}}$) for the suite of suitable foreground stars identified for each galaxy. The dispersions in these bootstrap calibrations range from 2% to 15% (with a median of 5%) and contribute to the overall photometric uncertainty estimates; the photometric uncertainties for the PS1-recalibrated fluxes are the sums in quadrature of these dispersions along with the uncertainties in the published $g_{\text{PS1}}r_{\text{PS1}}i_{\text{PS1}}z_{\text{PS1}} \rightarrow BVR_{\text{C}}I_{\text{C}}$ transformations and the instrumental galaxy flux measurements.

The *Pan-STARRS1* survey does not encompass regions of the sky south of Galactic latitude $\delta = -30^{\circ}$, and thus PS1 calibration is not possible for 18 SINGS/KINGFISH objects. Table 3 indicates for which targets the $BVR_{\text{C}}I_{\text{C}}$ photometry has been re-calibrated via PS1. Additional broadband optical photometry is possible via other ground-based efforts. *SDSS ugriz* imaging (Data Release 12) is used to provide optical fluxes for 51 of the 79 SINGS/KINGFISH galaxies. The union of the *SDSS ugriz* and PS1-recalibrated $BVR_{\text{C}}I_{\text{C}}$ samples comprises 63 galaxies, hence 80% of the full sample. The fraction of the sample for which we have reliable optical photometry approaches 100% after inclusion of $BVR_{\text{C}}I_{\text{C}}$ photometry from other global photometric datasets (see Table 3 and de Vaucouleurs et al. 1991; Muñoz-Mateos et al. 2009; Tully et al. 2009; Cook et al. 2014).

Other differences between our $BVR_{\text{C}}I_{\text{C}}$ photometry and those appearing in Dale et al. (2007) include the use of SINGS Data Release 5 (DR5) images (DR2 imaging was used in the previous publication), more robust sky level determinations (i.e., a significantly larger number of sky pixels are now used—38% more on average), and a fresh take on the editing of foreground stars and background galaxies (see § 3.5). In some instances the DR5 images are noticeably flatter than their DR2 counterparts (e.g., NGC 0628 $VR_{\text{C}}I_{\text{C}}$). Otherwise, the data processing procedures are essentially identical to those already described in Dale et al. (2007).

3.2. Herschel Infrared

Fluxes based on *Herschel* PACS and SPIRE imaging are presented here for 67 of the 79 SINGS/KINGFISH galaxies. The *Herschel* PACS and SPIRE imaging observations are described in Dale et al. (2012) for the 61 KINGFISH galaxies, except for the PACS observations of NGC 0584 which were taken too late to appear in that publication. Another minor difference from Dale et al. (2012) is that the PACS maps utilized here are deeper for five KINGFISH objects since we have now incorporated additional data from other observing programs: Holmberg II, IC 2574, NGC 2798, NGC 4236, and NGC 4631. Deeper observations allow for more robust measurements, e.g., the 70 and 100 μm flux-to-uncertainty ratios for Holmberg II are a factor of two larger than published in Dale et al. (2012) (see § 4). We also

incorporate here new *Herschel* imaging observations for six SINGS galaxies from the Herschel Very Nearby Galaxy Survey (VNGS; PI C. Wilson) that are not in the KINGFISH sample: NGC 2403, M81=NGC 3031, M82=NGC 3034, NGC 4125, M51a=NGC 5194, and M51b=NGC 5195. The observing procedures for these six galaxies are described in [Bendo et al. \(2010\)](#).

The *Herschel* PACS and SPIRE imaging data for these $61 + 6 = 67$ KINGFISH + VNGS galaxies for this publication were processed from Level 0 to Level 1 using HIPE Version 11.1.0¹, and the Level 1 to Level 2 post-pipeline processing utilized Scanamorphos Version 24.0 ([Roussel 2013](#)); the data published in [Dale et al. \(2012\)](#) were processed using HIPE Version 5.0 and Scanamorphos Version 12.5. With this newer version of Scanamorphos, the PACS distortion flatfield is now properly incorporated. In practice, this has decreased the noise levels in the PACS maps and slightly modified the PACS flux calibration ($\sim 1\%$). Moreover, the de-striping of PACS observations of large and diffuse fields is substantially improved, and the subtraction of the average drift on short timescales no longer introduces low-level noise. These changes allow for more secure detections of diffuse emission and more robust estimates of sky levels.

One important factor involved in the SPIRE flux calibration is the SPIRE beam size, since the SPIRE images are converted to surface brightness units by dividing by the estimated beam areas. The updated beam sizes used for this work at [250,350,500] μm are [469.35,831.27,1804.31]arcsec 2 , representing percentage increases of [11.0,10.7,13.7]\% compared to the previous values of [423,751,1587]arcsec 2 used by [Dale et al. \(2012\)](#). These updated values are the recommended beam sizes in Version 3.0 (03 June 2016) of the SPIRE Handbook.

The PACS fractional calibration uncertainties are of order $\epsilon_{\text{cal}}/f_\nu \sim 5\%$, according to Version 2.5.1 (09 July 2013) of the PACS Observer’s Manual. Calibration uncertainties for SPIRE data are estimated at $\epsilon_{\text{cal}}/f_\nu \sim 7\%$, also taken from Version 3.0 of the SPIRE Observer’s Manual. This level of uncertainty in the SPIRE calibration is a sum in quadrature of the uncertainties in the absolute and relative calibrations ($\sim 5.5\%$) along with the uncertainties in the extended source calibration ($\sim 4\%$).

3.3. WISE 12 μm

WISE 12 μm imaging ([Wright et al. 2010](#)) is utilized here to help bridge the gap in wavelength coverage in our broadband SEDs between the *Spitzer* 8 and 24 μm bandpasses. The 12 μm bandpass is an important tracer of the PAH complexes centered near (restframe) wavelengths of 11.3, 12.7, and 17 μm ([Smith et al. 2007](#)). At 12 μm , the (single-frame) *WISE* PSF full-width at half maximum (FWHM) is 6''.5 and the photometric calibration $\sim 7\%$ ². A full suite of *WISE* W1, W2, W3, and W4 (3.4, 4.6, 12, and 22 μm) “total” flux densities are provided in Table 4 (see the Appendix). We utilize native resolution imaging (not the drizzled Atlas release imaging) which provides superior resolution and minimizes the need for aperture corrections.

3.4. Planck 850 μm

There are SCUBA 850 μm flux densities available for only 27 galaxies in the SINGS/KINGFISH sample and so we supplement these data with *Planck* 850 μm flux densities for 36 galaxies; the total number of 850 μm detections for the combined *Planck*/SCUBA SINGS/KINGFISH sample is 43. We utilize cataloged *Planck* 850 μm flux densities derived from the APERFLUX technique, a technique that employs circular apertures plus concentric sky annuli. Among the different flavors of *Planck* flux density extractions, APERFLUX is the simplest method and relies on the fewest assumptions; the *Planck* team recommends APERFLUX for wavelengths 850 μm and shorter ([Planck Collaboration et al. 2016](#)). Though some of the SCUBA 850 μm data suffer from relatively small maps and spatial filtering issues, the lower-resolution *Planck* data may be impacted by foreground/background sources.

3.5. Sky Estimation and Elimination of Spatial Interlopers

The “sky” in the direction of any galaxy is a superposition of emission from faint foreground stars and background galaxies, interstellar emission, and in the case of ground-based observations, the Earth’s atmosphere. To determine the sky level for each image, a set of sky apertures has been defined (by eye) that collectively circumscribe the galaxy, projected on the sky close enough to the galaxy to measure the “local” sky but far enough away to avoid any galaxy emission (the process is unchanged from [Dale et al. 2012](#), see their Figure 1).

Prior to estimating the sky levels and executing aperture photometry, any emission from obvious foreground stars or neighboring/background galaxies is identified and removed from the areas covered by each galaxy’s aperture and

¹ Version 14.0.0 was used for the six VNGS galaxies. This version provides better deglitched SPIRE maps and a slightly improved extended source calibration for PACS.

² Explanatory Supplement to the WISE All-Sky Data Release Products; 19 February 2015

collection of sky apertures. The identification is assisted by ancillary data at shorter wavelengths and higher spatial resolution (e.g., *Spitzer*/IRAC 3.6 and 8.0 μm , *HST* optical, and ground-based H α imaging). The removal is accomplished via IRAF/IMEDIT by replacing the values of contaminated pixels via a 2D surface fit to a nearby sky annulus of width 2 pixels, with noise added that matches the noise statistics of the sky annulus. These annuli only sample the local sky around each spatial interloper and thus do not capture the full sky variations across the image. Fortunately, the spatial interlopers are much smaller than our target galaxies, a fact that limits the impact of any shortcomings in the contaminant removal procedure.

The total sky area, derived from the sum of the areas from all sky apertures, is typically significantly greater than that covered by the galaxy aperture itself, thereby limiting the contribution of uncertainty in the sky level to the overall error budget. The mean sky level per pixel is computed from the collection of these sky apertures, the value is scaled to the number of pixels in the galaxy aperture, and the result is subtracted off from the overall galaxy aperture counts.

3.6. Aperture Photometry

The elliptical apertures used for global photometry are listed in Table 1, and the same aperture is used to extract the flux at each wavelength. The apertures were chosen to encompass essentially all of the detectable emission at every wavelength (see also Dale et al. 2005, 2007, 2012). The average ratio of aperture major axis length $2a$ to the de Vaucouleurs D_{25} optical major axis is 1.45 (with a 1σ dispersion in this ratio of 0.45).

At the longest wavelengths where the imaging resolution is typically coarsest, a small portion of the galaxy emission may appear beyond the chosen apertures. Thus, for the *Spitzer* and *Herschel* photometry we utilize the aperture corrections described in Dale et al. (2007) and Dale et al. (2012). No aperture corrections were applied to the WISE photometry as they are negligible for the large apertures used here on native resolution imaging.

The uncertainties in the integrated photometry ϵ_{total} are computed as a combination in quadrature of the calibration uncertainty ϵ_{cal} and the measurement uncertainty ϵ_{sky} based on the measured sky fluctuations and the areas covered by the galaxy and the sum of the sky apertures, i.e.,

$$\epsilon_{\text{total}} = \sqrt{\epsilon_{\text{cal}}^2 + \epsilon_{\text{sky}}^2} \quad (3)$$

with

$$\epsilon_{\text{sky}} = \sigma_{\text{sky}} \Omega_{\text{pix}} \sqrt{N_{\text{pix}} + N_{\text{pix}}^2 / N_{\text{sky}}} \quad (4)$$

where σ_{sky} is the standard deviation of the sky surface brightness fluctuations, Ω_{pix} is the solid angle subtended per pixel, and N_{pix} and N_{sky} are the number of pixels in the galaxy and (the sum of) the sky apertures, respectively. For the few sources undetected by *Spitzer*, *Herschel*, or *WISE* imaging, 5σ upper limits are derived assuming a galaxy spans all N_{pix} pixels in the aperture,

$$f_{\nu}(5\sigma \text{ upper limit}) = 5 \epsilon_{\text{sky}}. \quad (5)$$

Based on our visual scrutiny of the imaging datasets from a given telescope, any images redward of a non-detection are also considered to yield non-detections.

The galaxy apertures, the sky apertures, and the foreground stellar masks are provided with the electronic version of the journal article.

4. RESULTS

4.1. Flux Densities

Table 2 presents the spatially-integrated flux densities for all 79 SINGS+KINGFISH galaxies for 30 photometric bands. In Table 5 we also supply global aperture photometry for the few cases where upper limits are provided in Table 2. The tabulated flux densities include aperture corrections (§ 3.6) and are *not* corrected for Galactic extinction. No color corrections have been applied to the data in Table 2. Some of the fluxes presented here remain unchanged from the values published elsewhere, for example 2MASS JHK_s, *Spitzer* IRAC and MIPS, SCUBA 850 μm , and VLA 20 cm photometry. However, if any differences exist between values published in multiple publications, precedence is given to the more recent published values, e.g., 2MASS and *Spitzer* photometry from the Local Volume Legacy publication of Dale et al. (2009) is given priority over the 2MASS and *Spitzer* photometry appearing in Dale et al. (2007).

Figure 2 provides a comparison of our updated optical fluxes with those presented in previous publications. The updated $VR_{\text{C}}I_{\text{C}}$ optical fluxes are generally in agreement, on average, with previously-published values, and the 1σ

scatters in the differences for these filters are \sim 0.2–0.3 mag. The differences with published B filter fluxes, however, show a locus of points indicating the literature data are typically 0.2 mag fainter than what we obtain after calibrating via *Pan-STARRS1*. There is also a second grouping of B data points, comprising nearly one-third of the total sample, that indicates the [Dale et al. \(2007\)](#) data are \sim 0.4 mag *brighter*; these may be cases where the B standard star calibration images for [Dale et al. \(2007\)](#) were either saturated or obtained in non-photometric conditions, both of which would lead to artificially faint standard star counts/sec and thus artificially bright galaxy fluxes.

Figure 3 provides a similar comparison for the *Herschel* far-infrared/submillimeter photometry. The updated SPIRE beam sizes are larger than those used in [Dale et al. \(2012\)](#) by [11,11,14]% at [250,350,500] μm , which naturally leads to fainter SPIRE fluxes. This decrease is evident in Figure 3, where the average SPIRE flux is \sim [8,5,16]% fainter at [250,350,500] μm than what appeared in [Dale et al. \(2012\)](#). For the five galaxies where we incorporated additional PACS data from other observing programs (Holmberg II, IC 2574, NGC 2798, NGC 4236, and NGC 4631; see § 3), the resulting PACS maps are deeper and thus allow for some diffuse flux to be additionally detected. For faint Holmberg II it makes an appreciable difference: the 70 and 100 μm global fluxes are now 40-50% larger.

4.2. The Spectral Energy Distributions

Figure 4 shows the observed infrared/sub-millimeter spectral energy distributions for the KINGFISH sample. Included in each panel, when available, are the *GALEX* far- and near-ultraviolet, BVR_{IC} and $ugriz$ optical, *2MASS* JHK_s near-infrared, *Spitzer* 3.6, 4.5, 5.8, 8.0, 24, 70, and 160 μm , *WISE* 12 μm , *Herschel* 70, 100, 160, 250, 350, and 500 μm , and *Planck* and SCUBA 850 μm fluxes.

The broadband spectral energy distributions displayed in Figure 4 are fitted with the models of [Draine & Li \(2007\)](#) over the wavelength range 3.6–500 μm , models based on mixtures of amorphous silicate and graphitic dust grains that effectively reproduce the average Milky Way extinction curve and are consistent with observations of PAH features and the variety of infrared continua in local galaxies. A total of four free parameters are utilized in the fits: the fraction q_{PAH} of the dust mass residing in polycyclic aromatic hydrocarbons (PAHs), the intensity U_{\min} of the interstellar radiation field that heats the general diffuse interstellar medium, and the fraction γ of the dust mass heated by more intense starlight distributions such as those arising from photodissociation regions (PDRs) in star-forming regions, the ratio of the stellar mass to the dust mass (M_{dust} is determined by the normalization of the SED model with the observed photometric data). The parameter q_{PAH} ranges between 0% and 12%, and U_{\min} can have values between 0.01 and 30. As was done for [Draine et al. \(2007\)](#) and [Dale et al. \(2012\)](#), we minimize the number of free parameters by fixing the maximum value of the interstellar radiation field ($U_{\max} = 10^6$) as well as the power-law exponent that governs the distribution of starlight intensities heating the dust ($\alpha = 2$). More details of these models may be found in [Draine & Li \(2007\)](#) and [Draine et al. \(2007\)](#).

The new SED fits here can be compared to what was obtained previously for the KINGFISH sample in [Dale et al. \(2012\)](#) with the outdated SPIRE photometric calibration. Figure 5 provides such a comparison for dust mass, PAH fraction, and the properties of the radiation field that is heating the dust. The two systematic differences, in the inferred dust mass and the diffuse radiation field intensity U_{\min} , are the result of the changes in the PACS and SPIRE calibrations—brighter at 70 and 100 μm and fainter at 250, 350, and 500 μm result in warmer interstellar dust and smaller overall dust masses. We note that, while recent results indicate a necessary change in the DL07 dust opacities ([Dalcanton et al. 2015](#); [Planck Collaboration et al. 2016](#)), we are consistently using the same (original) dust models from [Draine & Li \(2007\)](#) in the Figure 5 comparisons. The two outliers in q_{PAH} are the result of the inclusion of new PACS photometry for NGC 0584 and an improved sky estimate for NGC1291’s PACS 70 μm map, which led to a factor of \sim 2 smaller flux that is now in much better agreement with the *Spitzer* 70 μm flux.

As was mentioned in [Dale et al. \(2012\)](#), the faintest targets pose the most challenges to SED fitting. Spatial variations in the foreground cirrus amplify the relative uncertainty in the extracted fluxes for such targets. Even with our updated data processing and analysis, this situation remains essentially unchanged for galaxies like NGC 0584, DDO 053, M81 dwarf B, and Holmberg I. However, the addition of *WISE* fluxes to the SED fitting incrementally improves our confidence in the SED fits. A more detailed analysis of theoretical fits to these SEDs is presented in the companion paper ([Hunt et al. 2017](#)) and in [Draine et al. \(2017\)](#).

4.3. Sub-millimeter Excess

In [Dale et al. \(2012\)](#) we found an excess of submillimeter emission for several galaxies in the KINGFISH sample, where the observed 500 μm emission was measured to lie significantly above the model predictions based on [Draine & Li \(2007\)](#) fits to the observed 3.6–500 μm SEDs. The submillimeter excess $\xi(500\mu\text{m})$ was quantitatively defined in

Dale et al. (2012) as

$$\xi(500\mu\text{m}) = \frac{f_\nu(500\mu\text{m})_{\text{observed}} - f_\nu(500\mu\text{m})_{\text{model}}}{f_\nu(500\mu\text{m})_{\text{model}}}. \quad (6)$$

This excess was primarily found in low-metallicity galaxies: nine of the ten dwarf/irregular/Magellanic galaxies in the KINGFISH sample with 500 μm detections exhibited $\xi(500\mu\text{m}) > 0.60$. This result echoed similar claims of submillimeter excess in studies of M 33, the Magellanic Clouds, and other low-metallicity star-forming galaxies (Galliano et al. 2005; Planck Collaboration et al. 2011; Galametz et al. 2011; Gordon et al. 2014; Izotov et al. 2014; Hermelo et al. 2016). With the updated calibrations for our present dataset, including SPIRE calibration changes that result in 500 μm fluxes lower by an average of 16% (Figure 3), we still see submillimeter excesses in the sample but at lower significance. The average excess for dwarf/irregular/Magellanic galaxies in Dale et al. (2012) was $\langle \xi(500\mu\text{m}) \rangle_{T=\text{Im},\text{I0},\text{Sm}} \sim 0.70$, whereas in the current work the average value is $\langle \xi(500\mu\text{m}) \rangle_{T=\text{Im},\text{I0},\text{Sm}} \sim 0.53$ for the 11 SINGS/KINGFISH dwarf/irregular/Magellanic galaxies with secure 500 μm detections. Note that an alternative signal-to-noise-like definition of the submillimeter excess may be defined by normalizing via the model and observational uncertainties, namely

$$S/N(500\mu\text{m excess}) = \frac{f_\nu(500\mu\text{m})_{\text{observed}} - f_\nu(500\mu\text{m})_{\text{model}}}{\sqrt{\epsilon_{\text{obs}}^2 + \epsilon_{\text{mod}}^2}}. \quad (7)$$

In this case the average value is $\langle S/N(500\mu\text{m excess}) \rangle \sim 4.3$ for $\epsilon_{\text{mod}} = 0$ and ~ 3.3 for $\epsilon_{\text{mod}} = 0.1 f_\nu(500\mu\text{m})_{\text{model}}$ for the 11 SINGS/KINGFISH dwarf galaxies. We caution that our results may be biased since we restrict our analysis to securely-detected sources.

Though the lefthand panel of Figure 6 shows no dependence for submillimeter excess on far-infrared color, there is a clear trend in the righthand panel, with higher submillimeter excesses for lower gas-phase metallicity. This persistency of a submillimeter excess in primarily low-metallicity galaxies conflicts with the analysis of Kirkpatrick et al. (2013), who found no significant submillimeter excesses for a subset of 20 galaxies from the KINGFISH sample with robust (and updated) far-infrared photometry that span a range in metallicity. However, there are three main differences between the analysis carried out here and by Kirkpatrick et al. (2013). First, Kirkpatrick et al. (2013) only fit data spanning 24–350 μm . Our SED fitting employs the full infrared continuum over 3.6–500 μm and therefore our approach must balance contributions from stellar and PAH emission in addition to that from larger dust grains. Second, Kirkpatrick et al. (2013) employ the superposition of two modified blackbodies whereas our fits utilize a more sophisticated dust model (Draine & Li 2007); we have four free parameters in our SED fitting whereas Kirkpatrick et al. (2013) have only three free parameters: the temperature and emissivity of the cold dust component and the ratio of the amplitudes of the two modified blackbodies. Third, while we normalize our submillimeter excesses by the predicted model value at 500 μm , Kirkpatrick et al. (2013) normalize via the *observed* 500 μm value. Normalizing by the observed flux is an approach that naturally depresses the excess measure. For example, the average submillimeter excess for the 11 SINGS/KINGFISH dwarf/irregular/Magellanic galaxies with 500 μm detections is 0.33 if the normalization is via the observed flux, a factor of 1.6 times smaller than when normalizing by the predicted model flux.

5. SUMMARY

We present an update to the full panchromatic photometric database for the 79 galaxies in the combined SINGS/KINGFISH sample of nearby galaxies, for ultraviolet through radio wavelengths. Updates include incorporating recent improvements in the calibration of the *Herschel* photometers and a re-calibration of $BVR_{\text{C}}I_{\text{C}}$ photometry utilizing broadband data from the *Pan-STARRS1* survey. On average, the updated *Herschel* fluxes differ by $[+5,+8,0,-8,-5,-16]\%$ at $[70,100,160,250,350,500]\mu\text{m}$ compared to what was published in the original KINGFISH photometry paper of Dale et al. (2012). The average updated fluxes for the $V_{\text{R}}R_{\text{C}}I_{\text{C}}$ filters are essentially unchanged from the SINGS photometry presented in Dale et al. (2007), but with a scatter of 0.2–0.3 mag. The updated collection of B fluxes are about ~ 0.2 mag brighter than what appears in the literature. Finally, theoretical Draine & Li (2007) SED models are fit to each galaxy’s 3.6–500 μm dataset. Two of the fitted parameters show small but systematic differences with the results published previously: the total dust masses are about 3% smaller and the typical value of the radiation field that is heating the diffuse ISM is about 16% smaller. Both of these results naturally arise from the changes in the calibrations of the *Herschel* imagers since 2012. We confirm our previous finding of an excess of submillimeter emission (500 μm) in primarily low-metallicity dwarf/irregular galaxies, but at a smaller amplitude due to the updated calibration of the *Herschel* SPIRE beams. A full exploration of this panchromatic dataset is carried out in a companion paper by Hunt et al. (2017).

We thank the referee for excellent suggestions that improved this work. *Herschel* is an ESA space observatory with science instruments provided by European-led Principal Investigator consortia and with important participation from NASA. This work is based on observations made with the *Spitzer Space Telescope* and utilizes the NASA/IPAC Infrared Science Archive, both operated by JPL/Caltech under a contract with NASA. We gratefully acknowledge NASA's support for construction, operation, and science analysis for the GALEX mission, developed in cooperation with the Centre National d'Etudes Spatiales of France and the Korean Ministry of Science and Technology. Funding for the Sloan Digital Sky Survey and SDSS-II has been provided by the Alfred P. Sloan Foundation, the Participating Institutions, the NSF, the U.S. Department of Energy, NASA, the Japanese Monbukagakusho, the Max Planck Society, and the Higher Education Funding Council for England. This publication makes use of data products from the Wide-field Infrared Survey Explorer, which is a joint project of the University of California, Los Angeles, and the JPL/Caltech, funded by NASA. The Pan-STARRS1 Surveys have been made possible through contributions of the Institute for Astronomy, the University of Hawaii, the Pan-STARRS Project Office, the Max Planck Society and its participating institutes, the Max Planck Institute for Astronomy, Heidelberg and the Max Planck Institute for Extraterrestrial Physics, Garching, The Johns Hopkins University, Durham University, the University of Edinburgh, Queen's University Belfast, the Harvard-Smithsonian Center for Astrophysics, the Las Cumbres Observatory Global Telescope Network Incorporated, the National Central University of Taiwan, the Space Telescope Science Institute, the NSF, the University of Maryland, and Eotvos Lorand University and the Los Alamos National Laboratory.

APPENDIX

Appendix: WISE Fluxes

Table 2 presents WISE W3 (12 μm) flux densities based on the same apertures used for the other flux densities presented in Table 2. We additionally present here “total” flux densities for all four WISE bands using zeropoints of [309.666, 170.623, 29.043, 7.875] Jy for [W1, W2, W3, W4] at central wavelengths of [3.4, 4.6, 12, 22] μm ³. The process for extracting “total” flux densities follows that described in (Jarrett et al. 2013), whereby azimuthally-averaged elliptical surface brightness profiles are extrapolated to three disk scale lengths beyond the 1σ (sky rms) isophotal radii. For WISE, the 1σ isophotes are at surface brightness levels of approximately [23.0, 21.8, 18.1, 15.8] mag arcsec $^{-2}$ (Vega) for [W1, W2, W3, W4] (Jarrett et al. 2013). This particular WISE database provides an excellent opportunity to check our *Spitzer*- and aperture-based global fluxes at 3.6, 4.5, and 24 μm . Figure 7 presents such a comparison. The agreement between *Spitzer* and *WISE* flux densities is close to expectations. The dotted lines in the top two panels indicate the expected flux density ratios after convolving the filter bandpasses with a 5000 K stellar blackbody; the observed ratios match the expected ratios to within the observed 1σ scatters. There is perhaps a weak trend for the ratio of *Spitzer* 24 μm and *WISE* W3, with the ratio decreasing with increasing brightness.

REFERENCES

- Bendo, G. J., Wilson, C. D., Pohlen, M., et al. 2010, A&A, 518, L65
- Blanton, M. R., Schlegel, D. J., Strauss, M. A., et al. 2005, AJ, 129, 2562
- Boquien, M., Kennicutt, R., Calzetti, D., et al. 2016, A&A, 591, A6
- Brown, M. J. I., Jarrett, T. H., & Cluver, M. E. 2014, PASA, 31, HASH
- Chonis, T. S., & Gaskell, C. M. 2008, AJ, 135, 264
- Cook, D. O., Dale, D. A., Johnson, B. D., et al. 2014, MNRAS, 445, 899
- Cook, D. O., Dale, D. A., Johnson, B. D., et al. 2014, MNRAS, 445, 890
- Cook, D. O., Dale, D. A., Johnson, B. D., et al. 2014, MNRAS, 445, 881
- Cook, D. O., Dale, D. A., Lee, J. C., et al. 2016, MNRAS, 462, 3766
- da Cunha, E., Charlot, S., & Elbaz, D. 2008, MNRAS, 388, 1595
- Dalcanton, J. J., Fouesneau, M., Hogg, D. W., et al. 2015, ApJ, 814, 3
- Dale, D. A., Beltz-Mohrmann, G. D., Egan, A. A., et al. 2016, AJ, 151, 4
- Dale, D. A., Helou, G., Magdis, G. E., et al. 2014, ApJ, 784, 83
- Dale, D. A., Aniano, G., Engelbracht, C. W., et al. 2012, ApJ, 745, 95
- Dale, D. A., Barlow, R. J., Cohen, S. A., et al. 2010, ApJL, 712, L189
- Dale, D. A., Cohen, S. A., Johnson, L. C., et al. 2009, ApJ, 703, 517
- Dale, D. A., Smith, J. D. T., Schlafin, E. A., et al. 2009, ApJ, 693, 1821
- Dale, D. A., Barlow, R. J., Cohen, S. A., et al. 2008, AJ, 135, 1412
- Dale, D. A., Gil de Paz, A., Gordon, K. D., et al. 2008, ApJ, 672, 735-736
- Dale, D. A., Gil de Paz, A., Gordon, K. D., et al. 2007, ApJ, 655, 863
- Dale, D. A., Smith, J. D. T., Armus, L., et al. 2006, ApJ, 646, 228

³ Brown et al. (2014) suggest W4 has an effective central wavelength of 22.8 μm

- Dale, D. A., Bendo, G. J., Engelbracht, C. W., et al. 2005, ApJ, 633, 857
- Dale, D. A., Sheth, K., Helou, G., Regan, M. W., & Hüttemeister, S. 2005, AJ, 129, 2197
- Dale, D. A., Helou, G., Brauher, J. R., et al. 2004, ApJ, 604, 565
- Dale, D. A., Roussel, H., Contursi, A., et al. 2004, ApJ, 601, 813
- Dale, D. A., & Uson, J. M. 2003, AJ, 126, 675
- Dale, D. A., & Helou, G. 2002, ApJ, 576, 159
- Dale, D. A., Helou, G., Neugebauer, G., et al. 2001, AJ, 122, 1736
- Dale, D. A., Giovanelli, R., Haynes, M. P., Hardy, E., & Campusano, L. E. 2001, AJ, 121, 1886
- Dale, D. A., Helou, G., Contursi, A., Silbermann, N. A., & Kolhatkar, S. 2001, ApJ, 549, 215
- Dale, D. A., Silbermann, N. A., Helou, G., et al. 2000, AJ, 120, 583
- de Vaucouleurs, G., de Vaucouleurs, A., Corwin, H. G., Jr., et al. 1991, Third Reference Catalogue of Bright Galaxies. Volume I: Explanations and references. Volume II: Data for galaxies between 0^h and 12^h . Volume III: Data for galaxies between 12^h and 24^h .
- Draine, B. T., & Li, A. 2001, ApJ, 551, 807
- Draine, B. T. 2003, ARA&A, 41, 241
- Draine, B. T., Dale, D. A., Bendo, G., et al. 2007, ApJ, 663, 866
- Draine, B. T., & Li, A. 2007, ApJ, 657, 810
- Galametz, M., Madden, S., Galliano, F., et al. 2009, A&A, 508, 645
- Galametz, M., Madden, S. C., Galliano, F., et al. 2011, A&A, 532, A56
- Galametz, M., Kennicutt, R. C., Albrecht, M., et al. 2012, MNRAS, 425, 763
- Galametz, M., Kennicutt, R. C., Calzetti, D., et al. 2013, MNRAS, 431, 1956
- Galametz, M., Albrecht, M., Kennicutt, R., et al. 2014, MNRAS, 439, 2542
- Galliano, F., Madden, S. C., Jones, A. P., Wilson, C. D., & Bernard, J.-P. 2005, A&A, 434, 867
- Gordon, K. D., Roman-Duval, J., Bot, C., et al. 2014, ApJ, 797, 85
- Grier, C. J., Mathur, S., Ghosh, H., & Ferrarese, L. 2011, ApJ, 731, 60
- Hermelo, I., Relaño, M., Lisenfeld, U., et al. 2016, A&A, 590, A56
- Izotov, Y. I., Guseva, N. G., Fricke, K. J., Krügel, E., & Henkel, C. 2014, A&A, 570, A97
- Jarrett, T. H., Chester, T., Cutri, R., Schneider, S. E., & Huchra, J. P. 2003, AJ, 125, 525
- Jarrett, T. H., Masci, F., Tsai, C. W., et al. 2013, AJ, 145, 6
- Jester, S., Schneider, D. P., Richards, G. T., et al. 2005, AJ, 130, 873
- Jonsson, P., Groves, B. A., & Cox, T. J. 2010, MNRAS, 403, 17
- Jordi, K., Grebel, E. K., & Ammon, K. 2006, A&A, 460, 339
- Kartaltepe, J. S., Sanders, D. B., Le Floc'h, E., et al. 2010, ApJ, 709, 572
- Kennicutt, R. C., Jr., Armus, L., Bendo, G., et al. 2003, PASP, 115, 928
- Kennicutt, R. C., Calzetti, D., Aniano, G., et al. 2011, PASP, 123, 1347
- Kirkpatrick, A., Pope, A., Charmandaris, V., et al. 2013, ApJ, 763, 123
- Kirkpatrick, A., Calzetti, D., Galametz, M., et al. 2013, ApJ, 778, 51
- Kirkpatrick, A., Calzetti, D., Kennicutt, R., et al. 2014, ApJ, 789, 130
- Lupton, R. H., Jurić, M., Ivezić, Z., et al. 2005, Bulletin of the American Astronomical Society, 37, 133.08
- Magnier, E. A., Schlafly, E., Finkbeiner, D., et al. 2013, ApJS, 205, 20
- Maiolino, R., Carniani, S., Fontana, A., et al. 2015, MNRAS, 452, 54
- Moustakas, J., Kennicutt, R. C., Jr., Tremonti, C. A., et al. 2010, ApJS, 190, 233–266
- Muñoz-Mateos, J. C., Gil de Paz, A., Zamorano, J., et al. 2009, ApJ, 703, 1569–1596
- Muñoz-Mateos, J. C., Gil de Paz, A., Boissier, S., et al. 2009, ApJ, 701, 1965–1991
- Muñoz-Mateos, J. C., Sheth, K., Regan, M., et al. 2015, ApJS, 219, 3
- Noll, S., Burgarella, D., Giovannoli, E., et al. 2009, A&A, 507, 1793
- Planck Collaboration, Ade, P. A. R., Aghanim, N., et al. 2011, A&A, 536, A17
- Planck Collaboration, Ade, P. A. R., Aghanim, N., et al. 2016, A&A, 586, A132
- Planck Collaboration, Ade, P. A. R., Aghanim, N., et al. 2016, A&A, 594, A26
- Rémy-Ruyer, A., Madden, S. C., Galliano, F., et al. 2015, A&A, 582, A121
- Roussel, H. 2013, PASP, 125, 1126
- Schlafly, E. F., & Finkbeiner, D. P. 2011, ApJ, 737, 103
- Schlafly, E. F., Finkbeiner, D. P., Jurić, M., et al. 2012, ApJ, 756, 158
- Scolnic, D., Casertano, S., Riess, A., et al. 2015, ApJ, 815, 117
- Scoville, N., Sheth, K., Aussel, H., et al. 2016, ApJ, 820, 83
- Silva, L., Granato, G. L., Bressan, A., & Danese, L. 1998, ApJ, 509, 103
- Smith, J. D. T., Draine, B. T., Dale, D. A., et al. 2007, ApJ, 656, 770
- Smith, J. D. T., Croxall, K., Draine, B., et al. 2017, ApJ, 834, 5
- Tajer, M., Trinchieri, G., Wolter, A., et al. 2005, A&A, 435, 799
- Tonry, J. L., Stubbs, C. W., Lykke, K. R., et al. 2012, ApJ, 750, 99
- Tully, R. B., Rizzi, L., Shaya, E. J., et al. 2009, AJ, 138, 323
- Wright, E. L., Eisenhardt, P. R. M., Mainzer, A. K., et al. 2010, AJ, 140, 1868–1881

Table 1. Galaxy Sample

Galaxy	Alternative Name	Optical Morph.	$E(B - V)$ (mag.)	α_0 & δ_0 (J2000)	2a ('')	2b ('')	PA (°)	D (Mpc)	TIR (L_\odot)
NGC0024	UGC002	SAc	0.017	000955.9–245755	301	216	45	8.20	8.8
NGC0337	NGC0337	SBd	0.096	005950.7–073444	253	194	140	19.30	10.1
NGC0584	NGC0584	E4	0.036	013120.6–065205	326	278	60	20.80	8.7

Table 1 continued on next page

Table 1 (*continued*)

Galaxy	Alternative Name	Optical Morph.	$E(B - V)$ (mag.)	α_0 & δ_0 (J2000)	2a ($''$)	2b ($''$)	PA ($^{\circ}$)	D (Mpc)	TIR (L_{\odot})
NGC0628	Messier074	SAc	0.060	013642.4+154711	879	808	90	7.20	9.9
NGC0855	UGC01718	E	0.061	021403.7+275237	259	169	60	9.73	8.6
NGC0925	UGC01913	SABd	0.065	022713.6+333504	735	486	105	9.12	9.7
NGC1097	UGCA041	SBb	0.023	024618.0-301642	758	612	130	14.20	10.6
NGC1266	NGC1266	SB0	0.085	031600.6-022541	234	232	0	30.60	10.4
NGC1291	NGC1291	SB0/a	0.011	031717.9-410616	884	836	90	10.40	9.5
NGC1316	FornaxA	SAB0	0.018	032241.2-371210	864	583	50	21.00	9.9
NGC1377	NGC1377	S0	0.024	033639.0-205408	181	162	90	24.60	10.1
NGC1404	NGC1404	E1	0.010	033852.3-353540	524	369	149	20.20	...
IC0342	UGC02847	SABcd	0.480	034659.5+680539	1667	1439	100	3.28	10.1
NGC1482	NGC1482	SA0	0.034	035439.0-203009	349	310	119	22.60	10.6
NGC1512	NGC1512	SBab	0.009	040355.6-432149	1001	928	83	11.60	9.5
NGC1566		SABbc	0.008	042000.4-545615	552	435	40	18.00	10.6
NGC1705		SA0	0.007	045413.5-532137	167	120	40	5.80	8.0
NGC2146	UGC03429	Sbab	0.082	061835.6+782129	236	235	120	17.20	11.0
NGC2403	UGC03918	SABcd	0.034	073655.1+653534	1512	929	124	3.50	9.6
HolmbergII	UGC04305	Im	0.027	081910.8+704320	554	465	60	3.05	7.8
M081DwarfA		I?	0.018	082356.0+710145	78	78	90	3.50	...
DDO053	UGC04459	Im	0.033	083407.4+661043	155	142	90	3.61	7.0
NGC2798	UGC04905	SBa	0.017	091723.1+415957	235	232	90	25.80	10.6
NGC2841	UGC04966	SAb	0.013	092203.3+505837	629	334	150	14.10	10.1
NGC2915		I0	0.236	092609.4-763736	183	132	110	3.78	7.6
HolmbergI	UGC05139	IABm	0.044	094033.6+711120	264	219	63	3.90	7.1
NGC2976	UGC05221	SAc	0.062	094715.3+675509	541	353	144	3.55	8.9
NGC3049	UGC05325	SBab	0.033	095449.6+091614	218	160	29	19.20	9.5
NGC3031	Messier081	SAab	0.069	095531.8+690403	1628	1122	154	3.50	9.6
NGC3034	Messier082	I0	0.134	095552.1+694057	698	581	65	3.50	10.8
HolmbergIX	UGC05336	Im	0.068	095729.2+690250	247	180	40	3.50	...
NGC3077	UGC05398	I0pec	0.058	100317.5+684354	488	436	64	3.83	8.9
M081DwarfB	UGC05423	Im	0.068	100531.2+702151	134	90	139	3.60	6.5
NGC3190	UGC05559	SAap	0.022	101805.7+214957	334	196	117	19.30	9.8
NGC3184	UGC05557	SABcd	0.014	101815.6+412542	614	538	169	11.70	10.0
NGC3198	UGC05572	SBc	0.011	101954.8+453301	518	315	35	14.10	10.0
IC2574	UGC05666	SABm	0.031	102823.9+682505	864	486	59	3.79	8.3
NGC3265	UGC05705	E	0.021	103106.8+284751	184	175	50	19.60	9.4
Mrk33	UGC05720	Im	0.010	103231.2+542359	181	177	90	21.70	9.8
NGC3351	Messier095	SBb	0.024	104358.1+114210	592	441	11	9.33	9.9
NGC3521	UGC06150	SABbc	0.049	110548.1-000127	926	455	165	11.20	10.5
NGC3621	UGCA232	SAd	0.069	111818.3-324855	791	555	160	6.55	9.9
NGC3627	Messier066	SABb	0.029	112013.4+125927	745	486	167	9.38	10.4
NGC3773	UGC06605	SA0	0.023	113813.1+120644	118	116	0	12.40	8.8
NGC3938	UGC06856	SAc	0.018	115250.3+440715	504	468	0	17.90	10.3
NGC4125	UGC07118	E6p	0.016	120805.8+651024	228	151	90	21.40	9.1
NGC4236	UGC07306	SBdm	0.013	121643.2+692719	1240	369	162	4.45	8.7
NGC4254	Messier099	SAc	0.033	121849.7+142519	519	420	60	14.40	10.6
NGC4321	Messier100	SABbc	0.023	122254.8+154907	558	483	40	14.30	10.5
NGC4450	UGC07594	SAab	0.024	122830.1+170454	401	284	180	20.00	9.9
NGC4536	UGC07732	SABbc	0.016	123427.5+021113	454	376	120	14.50	10.3
NGC4552	Messier089	E	0.035	123539.8+123323	306	306	90	4.90	7.7
NGC4559	UGC07766	SABcd	0.015	123558.1+275752	576	327	140	6.98	9.5

Table 1 continued on next page

Table 1 (*continued*)

Galaxy	Alternative Name	Optical Morph.	$E(B - V)$ (mag.)	α_0 & δ_0 (J2000)	2a ($''$)	2b ($''$)	PA ($^{\circ}$)	D (Mpc)	TIR (L_{\odot})
NGC4569	Messier090	SABab	0.040	123650.2+131001	593	327	21	9.86	9.7
NGC4579	Messier058	SABb	0.035	123743.8+114858	325	271	90	16.40	10.1
NGC4594	Messier104	SAa	0.044	123959.6-113726	767	669	90	9.08	9.5
NGC4625	UGC07861	SABmp	0.016	124154.8+411623	298	214	100	9.30	8.8
NGC4631	UGC07865	SBd	0.015	124204.2+323219	901	240	85	7.62	10.4
NGC4725	UGC07989	SABab	0.010	125027.7+252948	689	523	30	11.90	9.9
NGC4736	Messier094	SAab	0.015	125055.2+410652	944	899	0	4.66	9.8
DDO154	UGC08024	IBm	0.008	125407.6+270916	216	126	50	4.30	...
NGC4826	Messier064	SAab	0.036	125643.3+214048	716	427	114	5.27	9.6
DDO165	UGC08201	Im	0.021	130625.9+674229	263	161	90	4.57	...
NGC5033	UGC08307	SAc	0.010	131328.2+363534	729	467	180	13.30	10.3
NGC5055	Messier063	SAbc	0.015	131549.2+420147	1097	711	80	7.94	10.3
NGC5194	Messier051a	SABbc	0.030	132950.6+471307	1699	1129	15	8.20	10.6
NGC5195	Messier051b	SB0p	0.031	132959.4+471556	202	191	0	8.20	9.3
NGC5398	Tololo89	SBdm	0.056	140121.2-330402	198	146	0	7.66	8.6
NGC5457	Messier101	SABcd	0.007	140325.0+542429	1800	1446	37	6.70	10.3
NGC5408		IBm	0.059	140321.1-412241	256	209	67	4.80	8.3
NGC5474	UGC09013	SAcd	0.009	140500.8+533920	412	373	90	6.80	8.7
NGC5713	UGC09451	SABbcP	0.034	144011.4-001726	225	225	90	21.40	10.5
NGC5866	UGC09723	S0	0.012	150628.8+554551	500	306	129	15.30	9.7
IC4710		SBm	0.076	182838.9-665903	313	219	120	8.50	8.6
NGC6822	DDO229	IBm	0.199	194453.2-144811	1453	1100	150	0.60	7.9
NGC6946	UGC11597	SABcd	0.294	203449.2+600959	953	928	0	6.80	10.5
NGC7331	UGC12113	SAb	0.078	223704.3+342435	683	335	168	14.50	10.7
NGC7552	IC5294	SAc	0.012	231610.8-423505	441	325	120	22.30	11.0
NGC7793		SAd	0.017	235749.9-323525	716	526	98	3.91	9.3

NOTE—Foreground extinctions derive from [Schlafly & Finkbeiner \(2011\)](#). 2a and 2b are the lengths of the major and minor axes used in the elliptical aperture photometry described herein; the position angle of the aperture's major axis is measured east of north. The total infrared luminosity listed in the last column is derived from Equation 5 of [Dale et al. \(2014\)](#) and the *Spitzer* 8, 24, 70, and 160 μm fluxes in Table 2 and assumes the distances provided in this table. *WISE* 22 μm and *Herschel* PACS 70 and 160 μm fluxes are used for NGC 3034 since its MIPS data suffer from saturation.

Table 2. Global Flux Densities in Janskys Corrected for Neither Galactic Nor Intrinsic Extinction

	GALEX		GALEX				SDSS		SDSS		SDSS	
Filter	FUV	NUV	B	V	R_C	I_C	u	g	r	i		
$\bar{\lambda}(\mu\text{m})$	0.154	0.231	0.441	0.551	0.659	0.806	0.356	0.482	0.626	0.767		
$\Delta\lambda(\mu\text{m})$	0.025	0.073	0.096	0.089	0.159	0.150	0.056	0.127	0.133	0.135		
A_λ/A_V	2.586	2.994	1.310	1.0	0.788	0.577	1.642	1.219	0.849	0.641		
NGC0024	772±121E-3	981±149E-3	817±021E-2	108±002E-1	138±007E-1	183±007E-1
NGC0337	463±064E-3	819±113E-3	786±046E-2	908±044E-2	108±006E-1	139±015E-1	249±006E-2	664±014E-2	100±002E-1	121±002E-1		
NGC0584	274±039E-4	146±020E-3	130±014E-1	264±020E-1	346±039E-1	519±048E-1	292±007E-2	143±002E-1	296±006E-1	433±008E-1		
NGC0628	469±073E-2	591±091E-2	528±033E-1	721±033E-1	921±042E-1	118±006E+0	179±003E-1	492±009E-1	804±016E-1	108±002E+0		
NGC0855	920±144E-4	178±027E-3	204±020E-2	335±033E-2	457±012E-2	...	840±029E-3	268±006E-2	468±010E-2	633±013E-2		
NGC0925	293±040E-2	357±049E-2	265±013E-1	456±123E-1	465±039E-1	601±049E-1
NGC1097	298±042E-2	418±058E-2	373±013E-1	641±023E-1	898±033E-1	124±004E+0
NGC1266	024±003E-4	141±019E-4	146±010E-2	289±015E-2	404±031E-2	638±047E-2
NGC1291	698±109E-3	151±023E-2	579±021E-1	118±004E+0	172±006E+0	241±008E+0
NGC1316	268±037E-3	142±019E-2	782±028E-1	155±005E+0	226±008E+0	290±010E+0
NGC1377	210±011E-2	350±014E-2	453±032E-2	732±023E-2
NGC1404	889±123E-4	253±035E-3	172±006E-1	355±013E-1	513±018E-1	764±028E-1
IC0342	233±034E-2	513±077E-2	975±134E-1
NGC1482	303±047E-4	106±015E-3	499±028E-2	692±045E-2	976±095E-2	150±013E-1
NGC1512	158±024E-2	165±028E-2	146±005E-1	252±009E-1	351±012E-1	489±018E-1
NGC1566	509±071E-2	612±084E-2	348±012E-1	593±021E-1	697±025E-1	864±031E-1
NGC1705	158±024E-2	148±022E-2	267±009E-2	366±013E-2	399±014E-2	537±019E-2
NGC2146	188±028E-3	485±072E-3	119±015E-1	210±027E-1	...	537±014E-1
NGC2403	185±029E-1	220±034E-1	129±012E+0	205±029E+0	227±008E+0	301±007E+0	751±015E-1	153±003E+0	225±004E+0	287±005E+0		
HoII	340±053E-2	369±056E-2	127±009E-1	149±007E-1	201±022E-1	303±049E-1
M81dwA	418±057E-4	488±067E-4	100±040E-3	900±400E-4	110±040E-3	140±060E-3
DDO053	214±033E-3	207±032E-3	660±160E-3	820±200E-3	550±180E-3	800±260E-3	271±014E-3	507±017E-3	602±020E-3	624±021E-3		
NGC2798	965±133E-4	201±027E-3	298±027E-2	545±033E-2	645±033E-2	110±010E-1	839±028E-3	310±007E-2	598±012E-2	825±017E-2		
NGC2841	116±016E-2	183±025E-2	435±020E-1	765±027E-1	101±007E+0	176±009E+0	111±002E-1	459±009E-1	941±018E-1	140±002E+0		
NGC2915	218±030E-3	216±030E-3	214±021E-2	308±011E-2	508±018E-2	500±050E-2
HoI	369±058E-3	401±061E-3	116±029E-2	153±038E-2	147±043E-2	211±053E-2
NGC2976	125±019E-2	173±026E-2	220±014E-1	357±011E-1	464±029E-1	676±045E-1	753±016E-2	225±004E-1	400±008E-1	539±010E-1		
NGC3049	228±034E-3	339±046E-3	246±020E-2	359±018E-2	397±028E-2	532±051E-2	923±027E-3	234±005E-2	390±008E-2	499±010E-2		
NGC3031	100±015E-1	133±020E-1	297±029E+0	610±061E+0	...	141±003E+1	884±017E-1	362±007E+0	778±015E+0	116±002E+1		
NGC3034	101±015E-2	288±043E-2	111±018E+0	164±016E+0	243±033E+0	376±045E+0	323±006E-1	105±002E+0	231±004E+0	345±006E+0		
HoIX	226±031E-3	280±038E-3	570±090E-3	550±110E-3	590±120E-3	900±300E-3	375±019E-3	635±020E-3	807±024E-3	930±028E-3		
NGC3077	183±005E-1	...	539±014E-1	...	694±015E-2	264±005E-1	496±010E-1	688±013E-1		
M81dwB	469±073E-4	586±090E-4	480±160E-3	650±210E-3	800±270E-3	830±230E-3	175±011E-3	447±016E-3	682±021E-3	842±025E-3		
NGC3190	334±046E-4	149±020E-3	997±040E-2	180±005E-1	253±008E-1	400±015E-1	216±005E-2	102±002E-1	211±004E-1	317±006E-1		
NGC3184	373±051E-2	492±068E-2	336±029E-1	478±020E-1	566±039E-1	740±041E-1	106±002E-1	316±006E-1	509±010E-1	667±013E-1		
NGC3198	215±029E-2	259±035E-2	200±008E-1	251±013E-1	296±024E-1	398±033E-1	628±013E-2	171±003E-1	270±005E-1	350±007E-1		
IC2574	390±061E-2	405±061E-2	140±019E-1	184±025E-1	182±029E-1	264±035E-1
NGC3265	474±065E-4	807±111E-4	112±014E-2	170±008E-2	218±020E-2	352±051E-2	365±016E-3	113±003E-2	209±005E-2	289±006E-2		
Mrk33	378±052E-3	475±065E-3	196±014E-2	283±055E-2	336±073E-2	392±078E-2	937±027E-3	197±004E-2	299±006E-2	342±007E-2		
NGC3351	147±023E-2	242±036E-2	302±037E-1	533±039E-1	700±050E-1	107±006E+0	876±018E-2	328±006E-1	620±012E-1	878±017E-1		
NGC3521	144±023E-2	296±045E-2	629±024E-1	107±002E+0	147±002E+0	225±006E+0	170±003E-1	664±013E-1	129±002E+0	180±003E+0		
NGC3621	427±062E-2	608±086E-2	428±015E-1	651±024E-1	780±028E-1	104±003E+0
NGC3627	246±038E-2	452±069E-2	742±042E-1	115±002E+0	141±012E+0	215±011E+0	214±004E-1	760±015E-1	136±002E+0	190±003E+0		
NGC3773	345±047E-3	454±062E-3	166±009E-2	226±008E-2	259±021E-2	327±026E-2	754±023E-3	163±004E-2	253±005E-2	307±007E-2		
NGC3938	...	311±043E-2	218±008E-1	308±005E-1	347±019E-1	486±017E-1	724±015E-2	203±004E-1	314±006E-1	407±008E-1		
NGC4125	...	193±028E-3	202±003E-1	369±007E-1	504±011E-1	764±048E-1	391±008E-2	204±004E-1	419±008E-1	619±012E-1		
NGC4236	625±098E-2	744±113E-2	343±029E-1	395±031E-1	479±038E-1	560±054E-1
NGC4254	259±038E-2	464±064E-2	344±021E-1	486±014E-1	614±022E-1	765±026E-1	128±002E-1	339±006E-1	543±010E-1	697±014E-1		
NGC4321	262±039E-2	445±061E-2	442±020E-1	670±017E-1	889±041E-1	132±007E+0	152±003E-1	442±008E-1	755±015E-1	103±002E+0		
NGC4450	...	438±060E-3	201±010E-1	368±010E-1	505±017E-1	768±032E-1	513±011E-2	213±004E-1	432±008E-1	629±012E-1		
NGC4536	148±020E-2	191±026E-2	185±012E-1	273±023E-1	343±035E-1	520±100E-1	561±012E-2	172±003E-1	292±005E-1	393±007E-1		
NGC4552	140±019E-3	344±047E-3	230±009E-1	425±010E-1	603±016E-1	942±051E-1	440±009E-2	239±004E-1	501±010E-1	749±015E-1		
NGC4559	473±065E-2	568±078E-2	305±019E-1	396±011E-1	452±033E-1	570±039E-1	108±002E-1	277±005E-1	402±008E-1	502±010E-1		
NGC4569	427±059E-3	139±019E-2	335±033E-1	555±055E-1	909±019E-2	361±007E-1	624±012E-1	900±018E-1		
NGC4579	434±060E-3	897±124E-3	293±012E-1	535±020E-1	694±043E-1	105±006E+0	661±014E-2	299±006E-1	602±012E-1	883±017E-1		
NGC4594	376±059E-3	111±017E-2	103±006E+0	242±032E+0	292±009E+0	453±028E+0	242±005E-1	123±002E+0	265±005E+0	401±008E+0		
NGC4625	549±087E-3	698±107E-3	364±028E-2	527±047E-2	617±086E-2	805±058E-2	126±003E-2	341±007E-2	534±011E-2	686±014E-2		
NGC4631	963±151E-2	118±018E-1	616±048E-1	812±030E-1	944±048E-1	119±005E+0	249±005E-1	579±011E-1	854±017E-1	108±002E+0		

Table 2 continued on next page

Table 2 (*continued*)

	<i>GALEX</i>	<i>GALEX</i>					<i>SDSS</i>	<i>SDSS</i>	<i>SDSS</i>	<i>SDSS</i>
Filter	FUV	NUV	B	V	R_C	I_C	u	g	r	i
$\bar{\lambda}(\mu\text{m})$	0.154	0.231	0.441	0.551	0.659	0.806	0.356	0.482	0.626	0.767
$\Delta\lambda(\mu\text{m})$	0.025	0.073	0.096	0.089	0.159	0.150	0.056	0.127	0.133	0.135
A_λ/A_V	2.586	2.994	1.310	1.0	0.788	0.577	1.642	1.219	0.849	0.641
NGC4725	202±028E-2	271±037E-2	466±024E-1	825±022E-1	104±003E+0	163±007E+0	123±002E-1	478±009E-1	910±018E-1	131±002E+0
NGC4736	625±098E-2	809±123E-2	141±009E+0	215±006E+0	292±010E+0	431±024E+0	415±008E-1	162±003E+0	300±006E+0	421±008E+0
DDO154	413±064E-3	401±062E-3	105±029E-2	113±035E-2	121±030E-2	127±032E-2	450±017E-3	892±026E-3	102±002E-2	102±002E-2
NGC4826	100±015E-2	258±039E-2	957±075E-1	149±008E+0	190±017E+0	303±017E+0	228±004E-1	966±019E-1	184±003E+0	268±005E+0
DDO165	483±075E-3	660±100E-3	285±071E-2	277±028E-2	254±055E-2	339±125E-2	929±028E-3	220±005E-2	255±006E-2	284±006E-2
NGC5033	181±025E-2	235±032E-2	241±012E-1	392±021E-1	...	636±041E-1	734±015E-2	235±004E-1	422±008E-1	581±011E-1
NGC5055	369±058E-2	586±090E-2	804±080E-1	133±013E+0	181±005E+0	274±007E+0	280±005E-1	934±018E-1	171±003E+0	245±004E+0
NGC5194	107±016E-1	165±025E-1	133±015E+0	182±012E+0	215±020E+0	323±029E+0	568±011E-1	149±003E+0	249±005E+0	335±006E+0
NGC5195	155±025E-3	420±066E-3	373±042E-1	612±041E-1	806±076E-1	150±013E+0	675±014E-2	261±005E-1	562±011E-1	852±017E-1
NGC5398	469±064E-3	699±096E-3	481±048E-2	506±050E-2	403±040E-2	520±052E-2
NGC5457	346±054E-1	387±059E-1	202±017E+0	261±024E+0	285±007E+0	431±011E+0	755±015E-1	189±003E+0	275±005E+0	352±007E+0
NGC5408	562±056E-2	804±080E-2
NGC5474	231±036E-2	251±038E-2	124±007E-1	165±006E-1	180±012E-1	215±019E-1	488±011E-2	116±002E-1	166±003E-1	199±004E-1
NGC5713	387±053E-3	750±103E-3	920±062E-2	134±006E-1	174±006E-1	237±025E-1	285±006E-2	884±018E-2	151±003E-1	197±004E-1
NGC5866	584±081E-4	375±051E-3	235±010E-1	429±015E-1	542±037E-1	849±049E-1	556±012E-2	255±005E-1	493±009E-1	731±014E-1
IC4710	118±016E-2	157±021E-2	566±056E-2	797±079E-2	704±070E-2
NGC6822	573±079E-2	739±103E-2	658±034E-1	973±037E-1	121±004E+0	977±085E-1
NGC6946	183±025E-2	335±046E-2	610±060E-1	127±005E+0	...	349±034E+0
NGC7331	802±111E-3	151±020E-2	452±026E-1	715±013E-1	101±002E+0	168±007E+0	905±019E-2	386±007E-1	814±016E-1	124±002E+0
NGC7552	697±096E-3	136±019E-2	127±004E-1	216±007E-1	226±022E-1	214±021E-1
NGC7793	111±017E-1	129±019E-1	550±055E-1	766±076E-1	745±074E-1	661±066E-1

NOTE—The compact table entry format $TUV \pm WXYZ$ implies $(T.UV \pm W.XY) \times 10^Z$ in Jy. Corrections for neither Galactic nor intrinsic extinction has been applied (see § 3). The uncertainties include both statistical and systematic effects. 5σ upper limits are provided for non-detections. No color corrections have been applied. The filter central wavelengths and widths are computed via Equations 1 and 2.

^aThe *Spitzer* MIPS data for NGC 3034 suffer from saturation and thus the tabulated values are lower limits.

Table 2. Global Flux Densities in Janskys Corrected for Neither Galactic Nor Intrinsic Extinction

	<i>SDSS</i>	<i>2MASS</i>	<i>2MASS</i>	<i>2MASS</i>	<i>Spitzer</i>	<i>Spitzer</i>	<i>Spitzer</i>	<i>Spitzer</i>	<i>WISE</i>	<i>Spitzer</i>
Filter	<i>z</i>	<i>J</i>	<i>H</i>	<i>K_S</i>	IRAC	IRAC	IRAC	IRAC	W3	MIPS
$\bar{\lambda}(\mu\text{m})$	0.910	1.24	1.65	2.17	3.56	4.51	5.76	7.96	12.8	23.8
$\Delta\lambda(\mu\text{m})$	0.131	0.163	0.252	0.264	0.687	0.872	1.25	2.55	5.51	5.32
A_{λ}/A_V	0.488	0.296	0.187	0.116	0.0451	0.0288	0.0193	0.0296	0.0355	0.0193
NGC0024	...	228±012E-1	246±013E-1	188±012E-1	101±013E-1	682±101E-2	821±116E-2	117±016E-1	924±064E-2	120±004E-1
NGC0337	136±002E-1	178±009E-1	190±009E-1	164±008E-1	958±126E-2	659±090E-2	141±018E-1	376±047E-1	291±020E-1	673±028E-1
NGC0584	562±011E-1	880±044E-1	109±005E+0	860±043E-1	365±049E-1	219±029E-1	174±022E-1	114±014E-1	700±049E-2	480±020E-2
NGC0628	123±002E+0	156±007E+0	160±008E+0	128±006E+0	839±117E-1	544±075E-1	116±014E+0	259±033E+0	235±016E+0	323±012E+0
NGC0855	766±017E-2	853±051E-2	940±064E-2	778±066E-2	428±060E-2	280±039E-2	359±030E-2	474±057E-2	354±024E-2	851±034E-2
NGC0925	...	561±028E-1	621±031E-1	500±026E-1	307±041E-1	210±028E-1	349±044E-1	606±075E-1	545±038E-1	943±040E-1
NGC1097	...	234±011E+0	270±013E+0	226±011E+0	123±016E+0	800±109E-1	146±018E+0	317±039E+0	298±020E+0	661±027E+0
NGC1266	...	112±005E-1	120±006E-1	116±006E-1	538±073E-2	414±054E-2	542±072E-2	878±111E-2	111±007E-1	872±036E-1
NGC1291	...	432±021E+0	453±022E+0	396±019E+0	207±028E+0	127±017E+0	906±121E-1	639±079E-1	592±041E-1	480±019E-1
NGC1316	...	461±023E+0	484±024E+0	417±020E+0	247±033E+0	153±021E+0	112±014E+0	553±069E-1	605±042E-1	428±021E-1
NGC1377	...	986±051E-2	113±006E-1	936±053E-2	567±075E-2	850±116E-2	267±035E-1	419±052E-1	397±027E-1	182±007E+0
NGC1404	...	136±006E+0	158±007E+0	134±006E+0	727±098E-1	434±059E-1	331±042E-1	158±020E-1	137±009E-1	880±040E-2
IC0342	...	952±047E+0	106±005E+1	107±005E+1	125±016E+1	701±096E+0	113±014E+1	251±031E+1	233±016E+1	362±014E+1
NGC1482	...	225±011E-1	294±015E-1	290±015E-1	204±028E-1	151±020E-1	592±076E-1	155±019E+0	123±008E+0	367±014E+0
NGC1512	...	804±043E-1	851±048E-1	727±046E-1	438±052E-1	294±033E-1	260±034E-1	456±054E-1	448±031E-1	486±019E-1
NGC1566	...	138±006E+0	140±007E+0	126±006E+0	750±101E-1	479±065E-1	907±115E-1	211±026E+0	188±013E+0	282±012E+0
NGC1705	...	570±036E-2	537±044E-2	442±047E-2	266±036E-2	192±025E-2	183±019E-2	192±020E-2	194±013E-2	538±022E-2
NGC2146	...	892±044E-1	117±005E+0	107±005E+0	835±113E-1	629±086E-1	250±032E+0	676±084E+0	495±034E+0	123±004E+1
NGC2403	329±006E+0	283±014E+0	284±014E+0	235±012E+0	149±025E+0	101±017E+0	197±026E+0	386±051E+0	395±027E+0	587±023E+0
HoII	...	275±016E-1	294±019E-1	226±018E-1	771±098E-2	644±078E-2	399±047E-2	440±048E-2	417±030E-2	177±007E-1
M81dwA	...	370±066E-3	384±098E-3	290±117E-3	185±094E-3	960±960E-4	<376E-3	<236E-3	<630E-4	<173E-2
DDO053	583±033E-3	730±200E-3	134±030E-2	783±366E-3	425±100E-3	309±100E-3	264±090E-3	437±100E-3	642±047E-3	239±010E-2
NGC2798	106±002E-1	160±008E-1	184±009E-1	172±009E-1	114±015E-1	810±114E-2	265±034E-1	632±078E-1	587±041E-1	261±010E+0
NGC2841	179±003E+0	277±013E+0	319±015E+0	265±013E+0	126±017E+0	750±103E-1	669±085E-1	115±014E+0	100±007E+0	908±037E-1
NGC2915	...	103±005E-1	127±006E-1	839±048E-2	521±072E-2	340±049E-2	321±043E-2	304±038E-2	180±012E-2	620±026E-2
HoI	...	296±041E-2	385±062E-2	157±072E-2	959±140E-3	595±120E-3	373±180E-3	362±160E-3	163±082E-3	654±073E-3
NGC2976	647±013E-1	808±040E-1	858±043E-1	689±036E-1	405±058E-1	281±039E-1	513±065E-1	101±012E+0	835±058E-1	139±005E+0
NGC3049	601±013E-2	751±040E-2	802±046E-2	729±045E-2	402±051E-2	273±038E-2	651±086E-2	134±016E-1	112±007E-1	426±017E-1
NGC3031	153±003E+1	219±010E+1	243±012E+1	207±010E+1	105±014E+1	652±089E+0	556±074E+0	759±099E+0	580±040E+0	521±020E+0
NGC3034	461±009E+0	811±040E+0	992±049E+0	960±048E+0	712±223E+0	567±178E+0	234±072E+1	613±189E+1	713±050E+1	322±096E+2 ^a
HoIX	902±060E-3	231±020E-2	196±027E-2	142±032E-2	730±113E-3	377±101E-3	<130E-2	<119E-2	526±050E-3	<362E-2
NGC3077	821±016E-1	993±050E-1	100±005E+0	850±044E-1	533±072E-1	360±049E-1	430±054E-1	808±100E-1	748±052E-1	129±005E+0
M81dwB	997±037E-3	111±014E-2	130±022E-2	132±026E-2	534±100E-3	360±100E-3	321±090E-3	307±080E-3	373±124E-3	332±034E-3
NGC3190	423±008E-1	697±034E-1	824±041E-1	734±036E-1	371±050E-1	234±032E-1	246±031E-1	327±041E-1	277±019E-1	266±011E-1
NGC3184	754±015E-1	103±005E+0	112±005E+0	908±046E-1	556±075E-1	356±048E-1	666±084E-1	143±017E+0	115±008E+0	142±005E+0
NGC3198	417±008E-1	568±028E-1	627±031E-1	545±027E-1	273±036E-1	173±023E-1	335±042E-1	682±085E-1	605±042E-1	105±004E+0
IC2574	...	360±020E-1	232±019E-1	172±021E-1	124±020E-1	906±127E-2	642±087E-2	688±089E-2	442±032E-2	281±011E-1
NGC3265	361±008E-2	497±028E-2	565±035E-2	476±035E-2	283±037E-2	198±026E-2	410±054E-2	101±012E-1	855±059E-2	294±012E-1
Mrk33	384±008E-2	486±028E-2	555±035E-2	476±035E-2	265±036E-2	188±026E-2	528±067E-2	127±016E-1	157±010E-1	861±035E-1
NGC3351	110±002E+0	164±008E+0	174±008E+0	152±007E+0	770±109E-1	500±070E-1	658±092E-1	126±016E+0	115±008E+0	253±010E+0
NGC3521	235±004E+0	355±017E+0	408±020E+0	342±017E+0	195±027E+0	129±018E+0	235±032E+0	559±075E+0	483±033E+0	548±021E+0
NGC3621	...	181±009E+0	205±010E+0	164±008E+0	983±132E-1	664±091E-1	160±020E+0	347±043E+0	293±020E+0	368±018E+0
NGC3627	236±004E+0	324±016E+0	366±018E+0	313±015E+0	177±025E+0	115±017E+0	219±030E+0	520±069E+0	460±032E+0	750±029E+0
NGC3773	345±008E-2	442±023E-2	380±022E-2	370±023E-2	221±027E-2	143±023E-2	255±034E-2	474±059E-2	409±028E-2	144±005E-1
NGC3938	464±009E-1	625±031E-1	570±029E-1	531±027E-1	320±043E-1	211±029E-1	410±052E-1	980±122E-1	846±059E-1	108±004E+0
NGC4125	795±016E-1	136±006E+0	151±007E+0	127±006E+0	639±086E-1	371±050E-1	247±032E-1	143±017E-1	104±007E-1	784±042E-2
NGC4236	...	626±033E-1	824±044E-1	566±034E-1	245±033E-1	185±028E-1	184±014E-1	215±027E-1	138±009E-1	513±020E-1
NGC4254	842±017E-1	122±006E+0	132±006E+0	119±006E+0	697±094E-1	468±064E-1	149±018E+0	392±048E+0	331±023E+0	419±016E+0
NGC4321	122±002E+0	182±009E+0	197±009E+0	163±008E+0	950±128E-1	637±087E-1	121±015E+0	287±035E+0	257±018E+0	333±013E+0
NGC4450	789±015E-1	117±005E+0	136±006E+0	106±005E+0	527±071E-1	324±044E-1	260±033E-1	267±033E-1	246±017E-1	209±011E-1
NGC4536	491±010E-1	702±035E-1	742±037E-1	694±035E-1	394±053E-1	285±038E-1	620±079E-1	165±020E+0	131±009E+0	345±013E+0
NGC4552	988±019E-1	157±007E+0	175±008E+0	143±007E+0	824±111E-1	480±065E-1	299±038E-1	170±021E-1	100±007E-1	940±041E-2
NGC4559	545±011E-1	760±038E-1	777±039E-1	652±033E-1	353±047E-1	233±032E-1	420±053E-1	837±104E-1	629±044E-1	111±004E+0
NGC4569	108±002E+0	175±008E+0	203±010E+0	164±008E+0	759±102E-1	472±064E-1	590±075E-1	101±012E+0	931±065E-1	143±005E+0
NGC4579	111±002E+0	198±009E+0	218±010E+0	179±008E+0	863±117E-1	520±071E-1	541±069E-1	726±090E-1	706±049E-1	759±031E-1
NGC4594	523±010E+0	771±038E+0	894±044E+0	743±037E+0	389±053E+0	235±031E+0	179±022E+0	144±016E+0	109±007E+0	771±030E-1
NGC4625	795±017E-2	966±063E-2	112±008E-1	892±087E-2	486±064E-2	307±040E-2	605±076E-2	134±016E-1	112±007E-1	128±005E-1
NGC4631	121±002E+0	172±008E+0	196±009E+0	182±009E+0	119±017E+0	845±114E-1	247±031E+0	584±072E+0	463±032E+0	812±032E+0

Table 2 continued on next page

Table 2 (*continued*)

Filter	<i>SDSS</i>	<i>2MASS</i>	<i>2MASS</i>	<i>2MASS</i>	<i>Spitzer</i>	<i>Spitzer</i>	<i>Spitzer</i>	<i>Spitzer</i>	WISE	<i>Spitzer</i>
	<i>z</i>	<i>J</i>	<i>H</i>	<i>K_S</i>	IRAC	IRAC	IRAC	IRAC	W3	MIPS
$\bar{\lambda}(\mu\text{m})$	0.910	1.24	1.65	2.17	3.56	4.51	5.76	7.96	12.8	23.8
$\Delta\lambda(\mu\text{m})$	0.131	0.163	0.252	0.264	0.687	0.872	1.25	2.55	5.51	5.32
A_{λ}/A_V	0.488	0.296	0.187	0.116	0.0451	0.0288	0.0193	0.0296	0.0355	0.0193
NGC4725	159±003E+0	240±012E+0	315±015E+0	239±012E+0	113±015E+0	704±096E-1	753±095E-1	120±015E+0	875±061E-1	859±037E-1
NGC4736	518±010E+0	684±034E+0	760±038E+0	639±032E+0	344±048E+0	229±031E+0	256±034E+0	481±064E+0	454±031E+0	552±022E+0
DDO154	126±004E-2	984±260E-3	123±039E-2	119±047E-2	510±100E-3	350±100E-3	<403E-3	<399E-3	<124E-3	<438E-3
NGC4826	336±006E+0	547±027E+0	616±030E+0	520±026E+0	239±034E+0	151±021E+0	159±021E+0	223±029E+0	185±012E+0	254±010E+0
DDO165	306±008E-2	313±035E-2	463±054E-2	370±062E-2	127±023E-2	907±150E-3	587±170E-3	407±080E-3	<168E-3	<448E-3
NGC5033	720±014E-1	119±006E+0	133±006E+0	116±005E+0	639±086E-1	470±064E-1	815±103E-1	192±023E+0	172±012E+0	196±007E+0
NGC5055	309±006E+0	414±020E+0	491±024E+0	402±020E+0	236±032E+0	155±021E+0	259±033E+0	558±070E+0	524±036E+0	558±022E+0
NGC5194	414±008E+0	484±024E+0	577±029E+0	446±022E+0	265±035E+0	178±025E+0	422±053E+0	106±013E+1	101±007E+1	124±004E+1
NGC5195	112±002E+0	229±011E+0	274±013E+0	222±011E+0	830±113E-1	509±070E-1	461±060E-1	644±080E-1	997±069E-1	146±005E+0
NGC5398	...	767±040E-2	644±037E-2	527±035E-2	375±050E-2	245±036E-2	143±020E-2	585±075E-2	641±044E-2	278±013E-1
NGC5457	386±007E+0	435±021E+0	501±025E+0	440±022E+0	281±038E+0	189±025E+0	338±042E+0	761±094E+0	687±048E+0	105±004E+1
NGC5408	...	124±006E-1	116±006E-1	742±050E-2	376±071E-2	214±051E-2	284±053E-2	254±047E-2	645±045E-2	427±017E-1
NGC5474	222±004E-1	262±014E-1	305±018E-1	193±015E-1	108±013E-1	730±102E-2	555±101E-2	114±014E-1	100±007E-1	156±006E-1
NGC5713	230±004E-1	362±018E-1	379±019E-1	327±016E-1	200±027E-1	137±019E-1	288±037E-1	114±014E+0	982±068E-1	234±009E+0
NGC5866	889±017E-1	129±006E+0	147±007E+0	125±006E+0	662±089E-1	420±057E-1	311±039E-1	314±039E-1	260±018E-1	213±008E-1
IC4710	...	997±054E-2	951±057E-2	753±054E-2	693±096E-2	461±064E-2	448±061E-2	644±082E-2	362±025E-2	118±005E-1
NGC6822	...	177±008E+0	184±009E+0	146±007E+0	157±027E+0	973±185E-1	988±179E-1	122±017E+0	110±007E+0	313±012E+0
NGC6946	...	546±027E+0	454±022E+0	502±025E+0	315±042E+0	212±029E+0	576±072E+0	137±017E+1	127±008E+1	199±007E+1
NGC7331	169±003E+0	264±013E+0	320±016E+0	273±013E+0	158±021E+0	101±013E+0	185±023E+0	401±049E+0	335±023E+0	434±024E+0
NGC7552	...	699±035E-1	791±039E-1	694±035E-1	452±061E-1	360±049E-1	106±013E+0	270±033E+0	266±018E+0	106±004E+1
NGC7793	...	164±008E+0	168±008E+0	130±006E+0	744±103E-1	481±064E-1	104±013E+0	189±023E+0	147±010E+0	209±008E+0

NOTE—The compact table entry format $TUV \pm WXYZ$ implies $(T.UV \pm W.XY) \times 10^Z$ in Jy. Corrections for neither Galactic nor intrinsic extinction has been applied (see § 3). The uncertainties include both statistical and systematic effects. 5 σ upper limits are provided for non-detections. No color corrections have been applied. The filter central wavelengths and widths are computed via Equations 1 and 2.

^aThe *Spitzer* MIPS data for NGC 3034 suffer from saturation and thus the tabulated values are lower limits.

Table 2. Global Flux Densities in Janskys Corrected for Neither Galactic Nor Intrinsic Extinction

	<i>Spitzer</i>	<i>Herschel</i>	<i>Herschel</i>	<i>Spitzer</i>	<i>Herschel</i>	<i>Herschel</i>	<i>Herschel</i>	<i>Herschel</i>	<i>JCMT</i>	<i>Planck</i>
Filter	MIPS	PACS	PACS	MIPS	PACS	SPIRE	SPIRE	SPIRE	SCUBA	HFI
$\bar{\lambda}(\mu\text{m})$	72.5	71.8	103	157	167	252	353	511	850	850
$\Delta\lambda(\mu\text{m})$	21.3	21.3	30.6	35.8	68.5	67.3	95.2	184	247	238
A_{λ}/A_V	0.00231	0.00231	0.00104	0.000388	0.000388	0.000152	0.0000725	0.0000361	0.0000146	0.0
NGC0024	222±015E+0	712±085E+0	457±091E-1
NGC0337	111±007E+1	139±006E+1	210±010E+1	200±024E+1	197±009E+1	894±063E+0	405±028E+0	158±011E+0	349±052E-1	573±234E-1
NGC0584	175±045E-1	180±025E-1	300±033E-1	118±030E+0	610±038E-1	<838E-1	<603E-1	<419E-1
NGC0628	338±023E+1	420±021E+1	836±041E+1	111±013E+2	114±005E+2	621±044E+1	298±021E+1	114±008E+1	...	198±015E+0
NGC0855	168±011E+0	208±010E+0	253±013E+0	222±026E+0	206±010E+0	135±009E+0	726±052E-1	222±018E-1
NGC0925	143±010E+1	136±006E+1	289±014E+1	433±052E+1	372±018E+1	251±017E+1	138±009E+1	652±046E+0
NGC1097	598±046E+1	787±039E+1	123±006E+2	153±018E+2	132±006E+2	669±047E+1	293±020E+1	106±007E+1	144±078E+0	212±012E+0
NGC1266	126±009E+1	148±007E+1	171±008E+1	102±012E+1	113±005E+1	404±028E+0	145±010E+0	402±030E-1
NGC1291	527±037E+0	439±027E+0	135±007E+1	262±031E+1	226±011E+1	151±010E+1	757±054E+0	309±022E+0
NGC1316	543±040E+0	568±029E+0	997±050E+0	126±017E+1	123±006E+1	494±035E+0	204±015E+0	707±058E-1
NGC1377	634±046E+0	725±036E+0	651±032E+0	338±042E+0	337±016E+0	122±008E+0	469±034E-1	163±013E-1
NGC1404	<165E-1	<214E-1	<252E-1	<286E-1	<204E-1	<154E-1	<134E-1	<909E-2
IC0342	351±024E+2	470±023E+2	894±044E+2	914±109E+2	107±005E+3	564±040E+2	251±017E+2	922±065E+1
NGC1482	324±028E+1	419±020E+1	522±026E+1	387±046E+1	419±021E+1	154±010E+1	582±041E+0	176±012E+0	330±050E-1	...
NGC1512	682±048E+0	752±039E+0	150±007E+1	196±023E+1	191±009E+1	147±010E+1	866±062E+0	363±026E+0	...	551±090E-1
NGC1566	343±025E+1	102±012E+2	142±010E+0
NGC1705	124±008E+0	139±016E+0
NGC2146	215±015E+2	198±009E+2	236±011E+2	119±014E+2	174±008E+2	613±043E+1	221±015E+1	681±048E+0
NGC2403	857±060E+1	994±049E+1	...	225±027E+2	192±009E+2	119±008E+2	627±048E+1	279±024E+1	...	422±032E+0
HoII	318±022E+0	438±022E+0	574±028E+0	346±042E+0	363±018E+0	152±011E+0	771±067E-1	284±142E-1
M81dwA	<149E-1	<143E-1
DDO053	315±025E-1	400±025E-1	519±031E-1	357±050E-1	300±020E-1	138±014E-1	989±106E-2	<389E-2
NGC2798	217±017E+1	250±012E+1	287±014E+1	206±024E+1	202±010E+1	740±052E+0	272±019E+0	853±061E-1	194±032E-1	...
NGC2841	102±007E+1	110±005E+1	286±014E+1	622±075E+1	488±024E+1	321±022E+1	152±010E+1	589±041E+0	...	122±010E+0
NGC2915	140±010E+0	107±005E+0	180±009E+0	145±026E+0	162±008E+0	816±059E-1	463±034E-1	204±016E-1
HoI	292±028E-1	280±031E-1	441±039E-1	526±075E-1	552±039E-1	369±031E-1	229±020E-1	108±012E-1
NGC2976	199±018E+1	209±010E+1	372±018E+1	426±051E+1	459±022E+1	242±017E+1	113±008E+1	442±031E+0	609±236E-1	110±022E+0
NGC3049	289±021E+0	382±019E+0	529±026E+0	486±059E+0	493±024E+0	259±018E+0	131±009E+0	644±046E-1
NGC3031	852±059E+1	997±049E+1	...	308±037E+2	281±014E+2	176±013E+2	876±070E+1	364±034E+1
NGC3034	162±048E+3 ^a	209±010E+3	...	857±257E+2 ^a	142±007E+3	442±031E+2	151±010E+2	456±033E+1	551±082E+0	900±018E+0
HoIX	<228E-1	<457E-1
NGC3077	196±013E+1	213±010E+1	292±014E+1	281±033E+1	278±013E+1	132±009E+1	613±043E+0	237±017E+0
M81dwB	114±012E-1	903±116E-2	270±018E-1	161±027E-1	292±018E-1	176±014E-1	104±010E-1	426±213E-2
NGC3190	565±040E+0	629±031E+0	109±005E+1	150±018E+1	153±007E+1	819±058E+0	348±024E+0	118±008E+0	189±035E-1	...
NGC3184	157±011E+1	180±009E+1	392±019E+1	704±084E+1	537±026E+1	314±022E+1	146±010E+1	577±041E+0	...	126±009E+0
NGC3198	102±007E+1	109±005E+1	224±011E+1	389±049E+1	296±014E+1	182±012E+1	955±067E+0	403±028E+0	...	105±010E+0
IC2574	483±034E+0	578±029E+0	937±047E+0	105±012E+1	986±049E+0	569±040E+0	412±029E+0	165±012E+0
NGC3265	270±019E+0	292±014E+0	322±016E+0	270±034E+0	285±014E+0	115±008E+0	509±037E-1	194±015E-1
Mrk33	434±031E+0	386±047E+0	400±060E-2	...
NGC3351	218±015E+1	270±013E+1	486±024E+1	569±068E+1	538±026E+1	313±022E+1	138±009E+1	480±034E+0	...	102±009E+0
NGC3521	644±045E+1	800±040E+1	163±008E+2	195±023E+2	203±010E+2	106±007E+2	459±032E+1	164±011E+1	210±082E+0	312±014E+0
NGC3621	501±039E+1	504±025E+1	101±005E+2	139±017E+2	124±006E+2	649±046E+1	305±021E+1	123±008E+1
NGC3627	918±070E+1	107±005E+2	188±009E+2	215±027E+2	196±009E+2	904±064E+1	360±025E+1	120±008E+1	186±070E+0	228±011E+0
NGC3773	157±012E+0	139±007E+0	214±010E+0	238±033E+0	206±010E+0	945±067E-1	414±030E-1	155±011E-1
NGC3938	142±010E+1	164±008E+1	307±015E+1	519±062E+1	392±019E+1	219±015E+1	983±069E+0	365±026E+0	...	883±083E-1
NGC4125	111±010E+0	740±041E-1	...	176±027E+0	183±009E+0	895±286E-1	509±210E-1	239±159E-1
NGC4236	801±056E+0	803±041E+0	113±005E+1	161±019E+1	172±008E+1	107±007E+1	694±049E+0	356±025E+0	...	727±101E-1
NGC4254	502±036E+1	596±029E+1	110±005E+2	142±017E+2	126±006E+2	618±043E+1	249±017E+1	833±059E+0	100±054E+0	159±009E+0
NGC4321	405±028E+1	440±022E+1	907±045E+1	139±016E+2	116±005E+2	627±044E+1	265±018E+1	901±064E+0	875±493E-1	165±008E+0
NGC4450	342±028E+0	169±021E+1
NGC4536	319±024E+1	419±020E+1	567±028E+1	580±070E+1	555±027E+1	268±019E+1	121±008E+1	462±032E+0	414±112E-1	967±078E-1
NGC4552	537±110E-1	142±073E+0
NGC4559	168±011E+1	180±009E+1	337±016E+1	541±065E+1	405±020E+1	236±016E+1	122±008E+1	529±037E+0	...	148±011E+0
NGC4569	123±008E+1	148±007E+1	325±016E+1	412±051E+1	400±020E+1	209±014E+1	900±063E+0	309±022E+0	464±082E-1	615±081E-1
NGC4579	952±075E+0	999±050E+0	254±012E+1	410±049E+1	345±017E+1	194±013E+1	844±059E+0	297±021E+0	439±066E-1	625±112E-1
NGC4594	730±051E+0	808±041E+0	259±013E+1	406±048E+1	380±019E+1	238±016E+1	116±008E+1	477±034E+0	372±108E-1	122±014E+0
NGC4625	185±013E+0	151±008E+0	376±019E+0	508±061E+0	469±023E+0	256±018E+0	130±009E+0	549±040E-1
NGC4631	138±009E+2	140±007E+2	233±011E+2	269±032E+2	238±011E+2	114±008E+2	523±037E+1	201±014E+1	573±120E+0	421±017E+0

Table 2 continued on next page

Table 2 (*continued*)

	<i>Spitzer</i>	<i>Herschel</i>	<i>Herschel</i>	<i>Spitzer</i>	<i>Herschel</i>	<i>Herschel</i>	<i>Herschel</i>	<i>Herschel</i>	<i>JCMT</i>	<i>Planck</i>
Filter	MIPS	PACS	PACS	MIPS	PACS	SPIRE	SPIRE	SPIRE	SCUBA	HFI
$\bar{\lambda}(\mu\text{m})$	72.5	71.8	103	157	167	252	353	511	850	850
$\Delta\lambda(\mu\text{m})$	21.3	21.3	30.6	35.8	68.5	67.3	95.2	184	247	238
A_{λ}/A_V	0.00231	0.00231	0.00104	0.000388	0.000388	0.000152	0.0000725	0.0000361	0.0000146	0.0
NGC4725	885±066E+0	103±005E+1	260±013E+1	599±073E+1	466±023E+1	302±021E+1	160±011E+1	648±046E+0	...	128±011E+0
NGC4736	100±007E+2	107±005E+2	165±008E+2	164±019E+2	141±007E+2	635±045E+1	260±018E+1	901±064E+0	153±065E+0	169±011E+0
DDO154	<591E-2	<775E-2	<912E-2	<223E-1	<801E-2	<514E-2	<483E-2	<349E-2
NGC4826	528±037E+1	563±028E+1	975±048E+1	857±102E+1	906±045E+1	393±027E+1	156±011E+1	516±036E+0	123±030E+0	101±008E+0
DDO165	<141E-1	<976E-2	<119E-1	<205E-1	<101E-1	<762E-2	<713E-2	<484E-2
NGC5033	288±020E+1	910±111E+1	109±055E+0	137±010E+0
NGC5055	744±052E+1	764±038E+1	175±008E+2	273±032E+2	241±012E+2	138±009E+2	611±043E+1	221±015E+1	...	397±015E+0
NGC5194	156±010E+2	180±009E+2	...	477±057E+2	409±020E+2	203±014E+2	831±064E+1	294±029E+1	261±039E+0	512±022E+0
NGC5195	971±068E+0	217±010E+1	...	129±015E+1	279±013E+1	123±009E+1	446±040E+0	152±022E+0	259±039E-1	...
NGC5398	203±015E+0	245±012E+0	333±016E+0	351±050E+0	283±014E+0	186±013E+0	101±007E+0	489±035E-1
NGC5457	118±008E+2	135±006E+2	262±013E+2	399±047E+2	336±016E+2	194±013E+2	942±066E+1	388±027E+1
NGC5408	358±026E+0	369±018E+0	275±014E+0	256±037E+0	231±011E+0	822±060E-1	416±032E-1	147±014E-1
NGC5474	347±024E+0	354±018E+0	604±031E+0	913±109E+0	853±043E+0	482±034E+0	280±020E+0	134±009E+0	...	377±085E-1
NGC5713	236±018E+1	295±014E+1	421±021E+1	396±047E+1	385±019E+1	156±011E+1	608±043E+0	193±013E+0	572±119E-1	500±116E-1
NGC5866	870±063E+0	880±044E+0	180±009E+1	177±021E+1	178±008E+1	757±053E+0	305±021E+0	965±072E-1	140±020E-1	192±067E-1
IC4710	237±018E+0	356±048E+0
NGC6822	636±044E+1	143±017E+2
NGC6946	206±016E+2	252±012E+2	457±022E+2	502±060E+2	525±026E+2	256±018E+2	106±007E+2	362±025E+1	298±044E+0	...
NGC7331	749±066E+1	688±034E+1	135±006E+2	189±024E+2	171±008E+2	882±062E+1	385±027E+1	139±009E+1	211±038E+0	...
NGC7552	675±110E+1	933±112E+1	795±166E-1	921±085E-1
NGC7793	329±023E+1	350±017E+1	695±034E+1	107±012E+2	901±045E+1	526±037E+1	276±019E+1	117±008E+1	...	283±013E+0

NOTE—The compact table entry format $TUV \pm WXYZ$ implies $(T.UV \pm W.XY) \times 10^Z$ in Jy. Corrections for neither Galactic nor intrinsic extinction has been applied (see § 3). The uncertainties include both statistical and systematic effects. 5σ upper limits are provided for non-detections. No color corrections have been applied. The filter central wavelengths and widths are computed via Equations 1 and 2.

^aThe *Spitzer* MIPS data for NGC 3034 suffer from saturation and thus the tabulated values are lower limits.

Table 3. $BVR_C I_C$ Photometry/Calibration
Source

Galaxy	<i>B</i>	<i>V</i>	R_C	I_C
NGC0024	PS1	PS1	PS1	PS1
NGC0337	PS1	PS1	PS1	PS1
NGC0584	PS1	PS1	PS1	PS1
NGC0628	PS1	PS1	PS1	PS1
NGC0855	RC3	RC3	C14	...
NGC0925	PS1	PS1	PS1	PS1
NGC1097	MM09	MM09	MM09	MM09
NGC1266	PS1	PS1	PS1	PS1
NGC1291	MM09	MM09	MM09	MM09
NGC1316	MM09	MM09	MM09	MM09
NGC1377	PS1	PS1	PS1	PS1
NGC1404	MM09	MM09	MM09	MM09
IC0342	RC3
NGC1482	PS1	PS1	PS1	PS1
NGC1512	MM09	MM09	MM09	MM09
NGC1566	MM09	MM09	MM09	MM09
NGC1705	MM09	MM09	MM09	MM09
NGC2403	PS1	PS1	PS1	PS1
NGC2146	RC3	RC3	...	T09
HolmbII	PS1	PS1	PS1	PS1
M81dwA	PS1	PS1	PS1	PS1
DDO053	PS1	PS1	PS1	PS1
NGC2798	PS1	PS1	PS1	PS1
NGC2841	PS1	PS1	PS1	PS1
NGC2915	RC3	MM09	MM09	D07
HolmbI	PS1	PS1	PS1	PS1
NGC2976	PS1	PS1	PS1	PS1
NGC3049	PS1	PS1	PS1	PS1
NGC3031	RC3	RC3	...	T09
NGC3034	PS1	PS1	PS1	PS1
HolmbIX	PS1	PS1	PS1	PS1
NGC3077	C14	...	RC3	...
M81dwB	PS1	PS1	PS1	PS1
NGC3190	PS1	PS1	PS1	PS1
NGC3184	PS1	PS1	PS1	PS1
NGC3198	PS1	PS1	PS1	PS1
IC2574	PS1	PS1	PS1	PS1
NGC3265	PS1	PS1	PS1	PS1
Mrk33	PS1	PS1	PS1	PS1
NGC3351	PS1	PS1	PS1	PS1
NGC3521	PS1	PS1	PS1	PS1
NGC3621	MM09	MM09	MM09	MM09
NGC3627	PS1	PS1	PS1	PS1
NGC3773	PS1	PS1	PS1	PS1
NGC3938	PS1	PS1	PS1	PS1
NGC4125	PS1	PS1	PS1	PS1
NGC4236	PS1	PS1	PS1	PS1
NGC4254	PS1	PS1	PS1	PS1

Table 3 continued on next page

Table 3 (*continued*)

Galaxy	<i>B</i>	<i>V</i>	<i>R_C</i>	<i>I_C</i>
NGC4321	PS1	PS1	PS1	PS1
NGC4450	PS1	PS1	PS1	PS1
NGC4536	PS1	PS1	PS1	PS1
NGC4552	PS1	PS1	PS1	PS1
NGC4559	PS1	PS1	PS1	PS1
NGC4569	RC3	RC3
NGC4579	PS1	PS1	PS1	PS1
NGC4594	PS1	PS1	PS1	PS1
NGC4625	PS1	PS1	PS1	PS1
NGC4631	PS1	PS1	PS1	PS1
NGC4725	PS1	PS1	PS1	PS1
NGC4736	PS1	PS1	PS1	PS1
DDO154	PS1	PS1	PS1	PS1
NGC4826	PS1	PS1	PS1	PS1
DDO165	PS1	PS1	PS1	PS1
NGC5033	PS1	PS1	...	PS1
NGC5055	RC3	RC3	C14	T09
NGC5194	PS1	PS1	PS1	PS1
NGC5195	PS1	PS1	PS1	PS1
NGC5398	D07	D07	D07	D07
NGC5457	RC3	RC3	C14	T09
NGC5408	RC3	RC3
NGC5474	PS1	PS1	PS1	PS1
NGC5713	PS1	PS1	PS1	PS1
NGC5866	PS1	PS1	PS1	PS1
IC4710	D07	D07	D07	...
NGC6822	PS1	PS1	PS1	PS1
NGC6946	RC3	PS1	...	PS1
NGC7331	PS1	PS1	PS1	PS1
NGC7552	MM09	MM09	D07	D07
NGC7793	D07	D07	D07	D07

NOTE—PS1: recalibration of [Dale et al. \(2007\)](#) photometry using Pan-STARRS1 (§3.1); D07: [Dale et al. \(2007\)](#); MM09: [Muñoz-Mateos et al. \(2009\)](#); C14: [Cook et al. \(2014\)](#); T09: unpublished photometry from M. Pierce via the Extragalactic Distance Database ([Tully et al. 2009](#)); RC3: [de Vaucouleurs et al. \(1991\)](#).

Table 4. WISE & VLA 20 cm Total Flux Densities in Janskys Corrected for Neither Galactic Nor Intrinsic Extinction

	WISE Filter	WISE W1	WISE W2	WISE W3	WISE W4	NRAO VLA 20 cm
	$\bar{\lambda}(\mu\text{m})$	3.40	4.65	12.8	22.4	
	$\Delta\lambda(\mu\text{m})$	0.663	1.04	5.51	4.11	
	A_{λ}/A_V	0.0523	0.0287	0.0285	0.0225	0.0
NGC0024	108±007E-1	544±039E-2	893±064E-2	111±009E-1	...	
NGC0337	977±069E-2	670±048E-2	308±022E-1	724±051E-1	109±010E-1	
NGC0584	420±029E-1	208±015E-1	661±107E-2	335±059E-2	<500E-2	
NGC0628	842±059E-1	512±037E-1	232±016E+0	326±023E+0	172±017E-1	
NGC0855	441±031E-2	245±017E-2	379±028E-2	731±055E-2	490±050E-3	
NGC0925	302±021E-1	176±012E-1	516±037E-1	856±066E-1	460±050E-2	
NGC1097	126±008E+0	766±055E-1	293±037E+0	685±083E+0	414±041E-1	
NGC1266	557±039E-2	398±029E-2	935±067E-2	725±051E-1	116±012E-1	
NGC1291	228±016E+0	120±008E+0	580±045E-1	492±048E-1	...	
NGC1316	296±020E+0	151±010E+0	525±037E-1	423±031E-1	255±026E-1	
NGC1377	503±035E-2	948±068E-2	393±027E-1	160±011E+0	<100E-3	
NGC1404	723±051E-1	372±027E-1	159±012E-1	719±061E-2	390±060E-3	
IC0342	831±058E+0	498±036E+0	250±018E+1	434±030E+1	240±024E+0	
NGC1482	207±014E-1	152±010E-1	119±008E+0	352±024E+0	238±024E-1	
NGC1512	401±028E-1	207±015E-1	386±027E-1	474±034E-1	700±100E-3	
NGC1566	740±052E-1	446±032E-1	188±022E+0	292±034E+0	400±000E-1	
NGC1705	296±021E-2	163±011E-2	204±036E-2	514±085E-2	...	
NGC2146	875±061E-1	660±047E-1	544±038E+0	161±011E+1	107±010E+0	
NGC2403	170±012E+0	104±007E+0	374±026E+0	610±043E+0	330±033E-1	
HeII	197±028E-2	
M81dwA	080±010E-4	
DDO053	460±034E-3	297±026E-3	617±063E-3	338±050E-2	...	
NGC2798	107±007E-1	763±055E-2	567±040E-1	237±016E+0	829±085E-2	
NGC2841	139±009E+0	763±055E-1	895±063E-1	111±008E+0	840±086E-2	
NGC2915	542±038E-2	301±021E-2	227±017E-2	524±041E-2	...	
HeI	
NGC2976	433±030E-1	255±018E-1	862±061E-1	140±009E+0	508±054E-2	
NGC3049	398±028E-2	225±016E-2	108±007E-1	384±027E-1	120±023E-2	
NGC3031	112±007E+1	619±044E+0	527±037E+0	491±035E+0	379±037E-1	
NGC3034	733±051E+0	614±044E+0	713±067E+1	356±031E+2	765±077E+0	
HeIX	
NGC3077	615±043E-1	356±025E-1	732±099E-1	182±024E+0	...	
M81dwB	559±040E-3	327±026E-3	
NGC3190	377±026E-1	214±015E-1	265±018E-1	259±019E-1	430±047E-2	
NGC3184	505±035E-1	289±020E-1	113±008E+0	146±010E+0	559±059E-2	
NGC3198	285±020E-1	168±012E-1	597±042E-1	102±007E+0	270±034E-2	
IC2574	113±008E-1	735±053E-2	441±038E-2	...	107±023E-2	
NGC3265	262±018E-2	155±011E-2	796±056E-2	266±019E-1	111±023E-2	
Mrk33	259±018E-2	172±012E-2	144±010E-1	788±055E-1	172±026E-2	
NGC3351	815±057E-1	434±031E-1	115±008E+0	246±017E+0	438±048E-2	
NGC3521	208±014E+0	121±008E+0	486±054E+0	597±066E+0	356±035E-1	
NGC3621	883±064E-1	533±041E-1	276±019E+0	367±026E+0	197±019E-1	
NGC3627	188±013E+0	112±008E+0	460±032E+0	794±056E+0	457±045E-1	
NGC3773	210±014E-2	121±008E-2	399±074E-2	124±021E-1	580±050E-3	
NGC3938	315±022E-1	197±014E-1	849±060E-1	112±008E+0	617±065E-2	
NGC4125	793±056E-1	399±028E-1	127±009E-1	674±059E-2	<500E-2	
NGC4236	229±016E-1	124±008E-1	134±013E-1	...	281±034E-2	
NGC4254	683±048E-1	445±032E-1	332±042E+0	448±056E+0	421±041E-1	
NGC4321	100±007E+0	625±045E-1	258±032E+0	378±047E+0	340±034E-1	
NGC4450	552±039E-1	295±021E-1	221±016E-1	224±019E-1	940±100E-3	
NGC4536	422±029E-1	267±019E-1	132±017E+0	349±041E+0	194±018E-1	
NGC4552	918±064E-1	447±032E-1	256±038E-1	999±160E-2	100±003E-1	
NGC4559	354±025E-1	232±016E-1	672±047E-1	123±009E+0	654±068E-2	
NGC4569	792±056E-1	451±032E-1	893±063E-1	139±009E+0	834±086E-2	
NGC4579	934±066E-1	503±036E-1	624±044E-1	721±052E-1	984±100E-2	
NGC4594	444±031E+0	236±017E+0	114±008E+0	893±069E-1	136±014E-1	
NGC4625	477±033E-2	277±020E-2	992±071E-2	136±011E-1	710±210E-3	

Table 4 continued on next page

Table 4 (*continued*)

	<i>WISE</i>	<i>WISE</i>	<i>WISE</i>	<i>WISE</i>	NRAO
Filter	W1	W2	W3	W4	VLA
$\bar{\lambda}(\mu\text{m})$	3.40	4.65	12.8	22.4	20 cm
$\Delta\lambda(\mu\text{m})$	0.663	1.04	5.51	4.11	
A_{λ}/A_V	0.0523	0.0287	0.0285	0.0225	0.0
NGC4631	124±008E+0	804±058E-1	469±051E+0	839±090E+0	120±012E+0
NGC4725	116±008E+0	598±043E-1	740±088E-1	721±084E-1	280±034E-2
NGC4736	389±027E+0	221±016E+0	447±055E+0	586±071E+0	270±027E-1
DDO154	443±032E-3
NGC4826	262±018E+0	142±010E+0	197±014E+0	262±018E+0	101±009E-1
DDO165	124±008E-2
NGC5033	643±045E-1	388±028E-1	167±011E+0	210±015E+0	178±017E-1
NGC5055	248±017E+0	140±010E+0	516±036E+0	628±044E+0	389±039E-1
NGC5194	288±020E+0	177±012E+0	977±069E+0	...	149±015E+0
NGC5195	814±057E-1	456±032E-1	582±041E-1	122±008E+0	495±053E-2
NGC5398	394±028E-2	210±015E-2	655±047E-2	265±019E-1	420±080E-3
NGC5457	254±018E+0	156±011E+0	658±046E+0	104±007E+1	749±075E-1
NGC5408	336±023E-2	196±014E-2	606±043E-2	458±033E-1	...
NGC5474	113±008E-1	638±046E-2	971±075E-2	135±012E-1	120±023E-2
NGC5713	205±014E-1	136±009E-1	988±069E-1	235±016E+0	159±016E-1
NGC5866	705±049E-1	387±027E-1	250±017E-1	226±016E-1	227±030E-2
IC4710	602±042E-2	349±025E-2
NGC6822	160±011E+0	873±063E-1	139±013E+0	286±027E+0	694±140E-2
NGC6946	310±021E+0	202±014E+0	122±014E+1	205±024E+1	139±014E+0
NGC7331	163±011E+0	982±070E-1	335±023E+0	429±030E+0	372±037E-1
NGC7552	440±031E-1	347±025E-1	270±035E+0	114±014E+1	275±028E-1
NGC7793	773±054E-1	463±033E-1	148±010E+0	184±013E+0	102±009E-1

NOTE—The compact table entry format TUV±WXYEZ implies $(T.UV \pm W.XY) \times 10^Z$ in Jy. Corrections for neither Galactic nor intrinsic extinction has been applied. The uncertainties include both statistical and systematic effects. No color corrections have been applied. The filter central wavelengths and widths are computed via Equations 1 and 2.

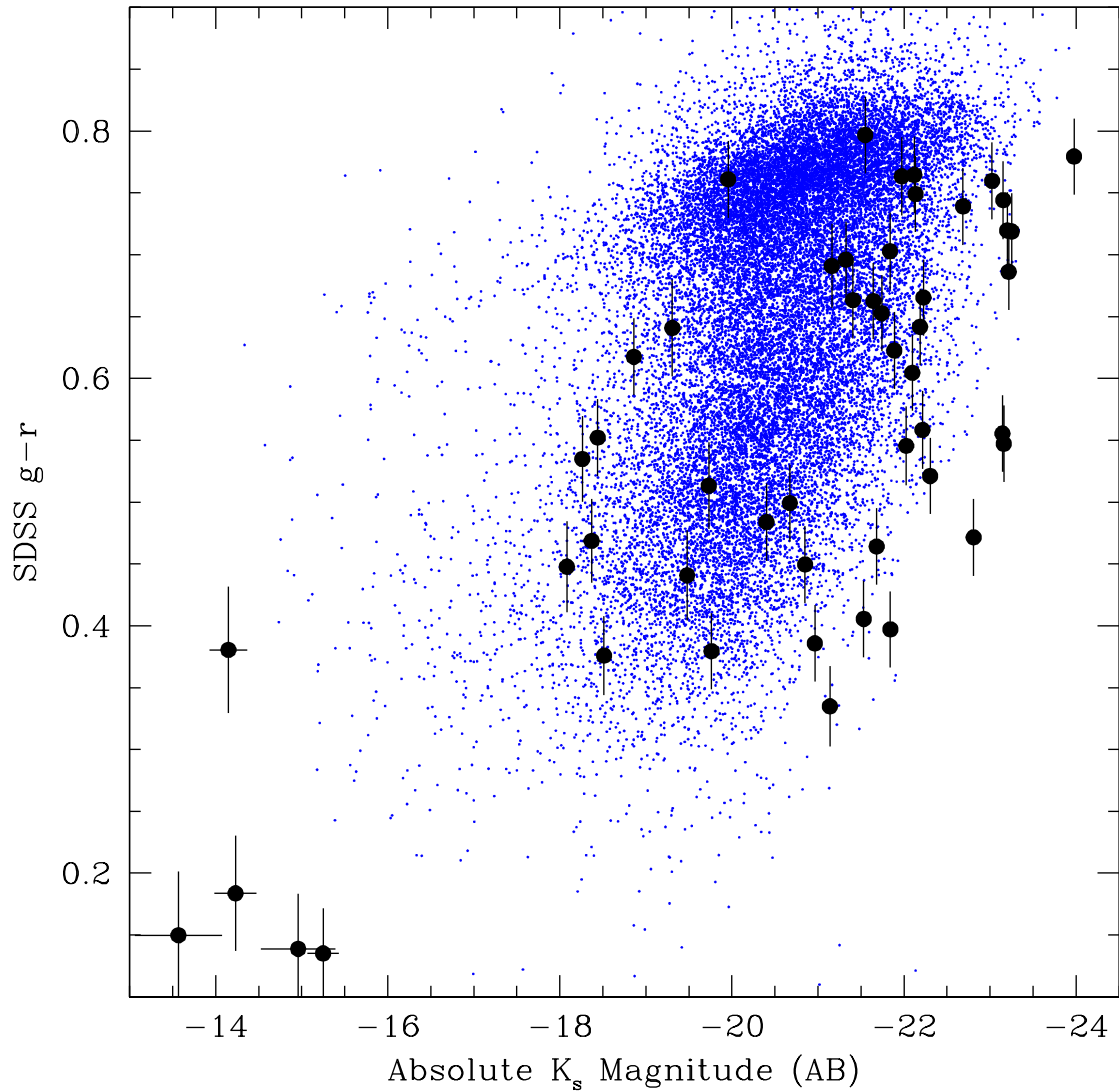


Figure 1. Comparison of global $g - r$ colors and absolute 2MASS K_s magnitudes for the KINGFISH/SINGS (large circles) and SDSS low redshift samples ($10 < d < 150$ Mpc h^{-1} ; Blanton et al. 2005). The values are corrected for foreground Milky Way extinction.

Table 5. Aperture Photometry for Cases of Upper Limits in Table 2

	<i>Spitzer</i>	<i>Spitzer</i>	<i>WISE</i>	<i>Spitzer</i>	<i>Spitzer</i>	<i>Herschel</i>	<i>Herschel</i>	<i>Spitzer</i>	<i>Herschel</i>	<i>Herschel</i>	<i>Herschel</i>	<i>Herschel</i>
Filter	IRAC	IRAC	W3	MIPS	MIPS	PACS	PACS	MIPS	PACS	SPIRE	SPIRE	SPIRE
$\bar{\lambda}(\mu\text{m})$	5.76	7.96	12.8	23.8	72.5	71.8	103	157	167	252	353	511
NGC0584	$281 \pm 158\text{E-}1$	$110 \pm 106\text{E-}1$	$099 \pm 684\text{E-}2$
NGC1404	$110 \pm 080\text{E-}1$	$330 \pm 062\text{E-}1$	$-111 \pm 009\text{E+}0$	$130 \pm 120\text{E-}1$	$630 \pm 066\text{E-}1$	$-149 \pm 030\text{E-}1$	$-139 \pm 025\text{E-}1$	$295 \pm 166\text{E-}2$
M81dwA	$-010 \pm 520\text{E-}3$	$034 \pm 640\text{E-}3$	$-420 \pm 090\text{E-}4$	$050 \pm 330\text{E-}3$	$029 \pm 146\text{E-}1$	$330 \pm 090\text{E-}2$...	$020 \pm 473\text{E-}1$
DDO053	$980 \pm 578\text{E-}3$
HoIX	$-400 \pm 200\text{E-}4$	$771 \pm 100\text{E-}3$	$526 \pm 050\text{E-}3$	$128 \pm 040\text{E-}3$	$068 \pm 120\text{E-}2$	$-251 \pm 260\text{E-}2$
DDO154	$560 \pm 080\text{E-}3$	$180 \pm 200\text{E-}4$	$422 \pm 035\text{E-}3$	$145 \pm 050\text{E-}3$	$338 \pm 140\text{E-}2$	$-270 \pm 019\text{E-}1$	$500 \pm 029\text{E-}1$	$-009 \pm 280\text{E-}2$	$600 \pm 136\text{E-}2$	$109 \pm 011\text{E-}1$	$693 \pm 093\text{E-}2$	$294 \pm 061\text{E-}2$
DDO165	$800 \pm 280\text{E-}4$	$449 \pm 060\text{E-}3$	$141 \pm 020\text{E-}1$	$-240 \pm 021\text{E-}1$	$150 \pm 022\text{E-}1$	$206 \pm 043\text{E-}1$	$400 \pm 178\text{E-}2$	$101 \pm 133\text{E-}2$	$100 \pm 124\text{E-}2$	$501 \pm 092\text{E-}2$

NOTE—The compact table entry format $TUV \pm WXYZ$ implies $(T.UV \pm W.XY) \times 10^Z$ in Jy. Corrections for neither Galactic nor intrinsic extinction has been applied (see § 3). The uncertainties include both statistical and systematic effects. No color corrections have been applied.

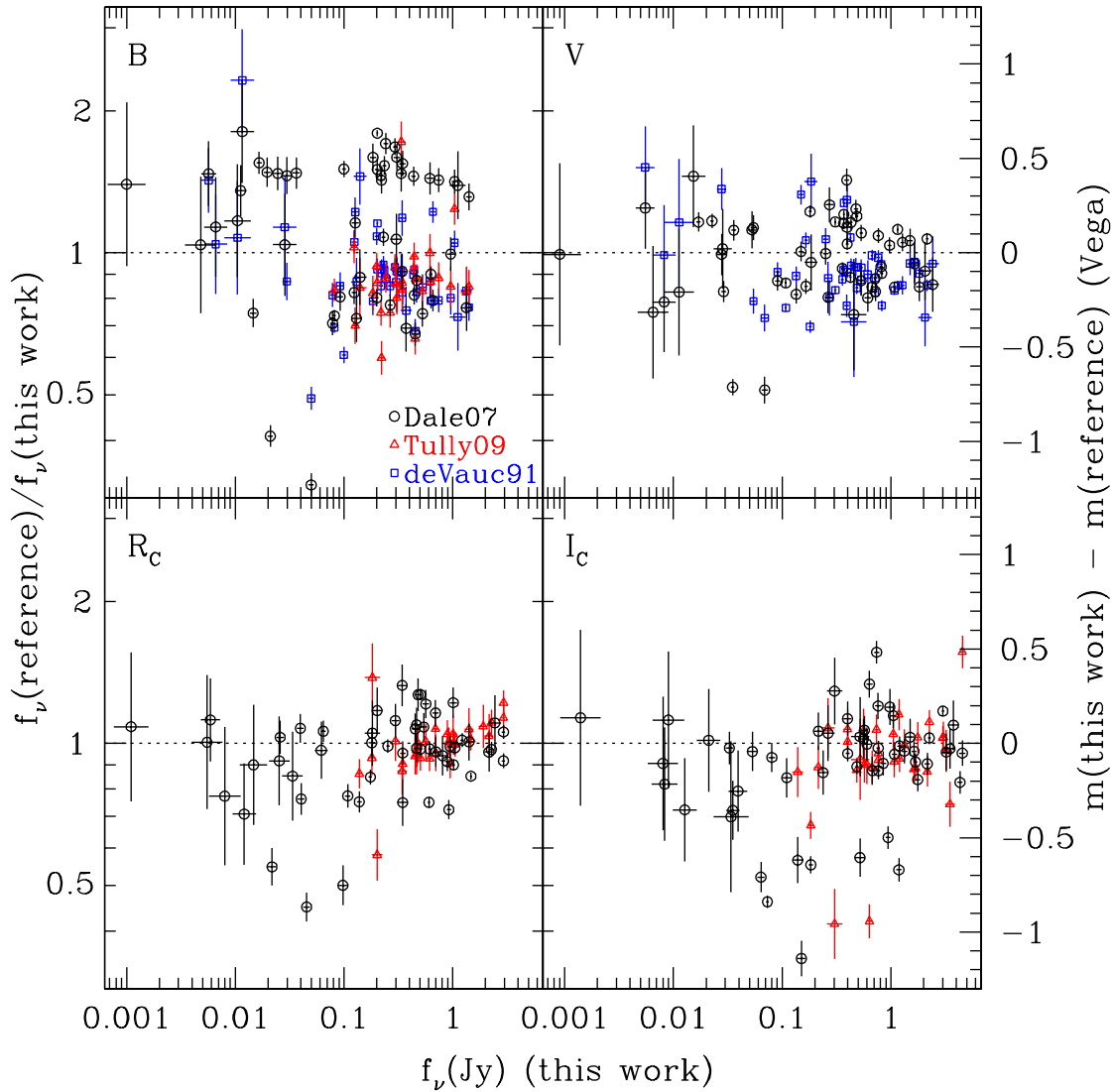


Figure 2. Comparison of global BVR_CI_C galaxy photometry from the literature with those measured here which are calibrated based on Pan-STARRS1 $g_{P1}r_{P1}i_{P1}z_{P1}$ photometry on field stars (see § 3.1).

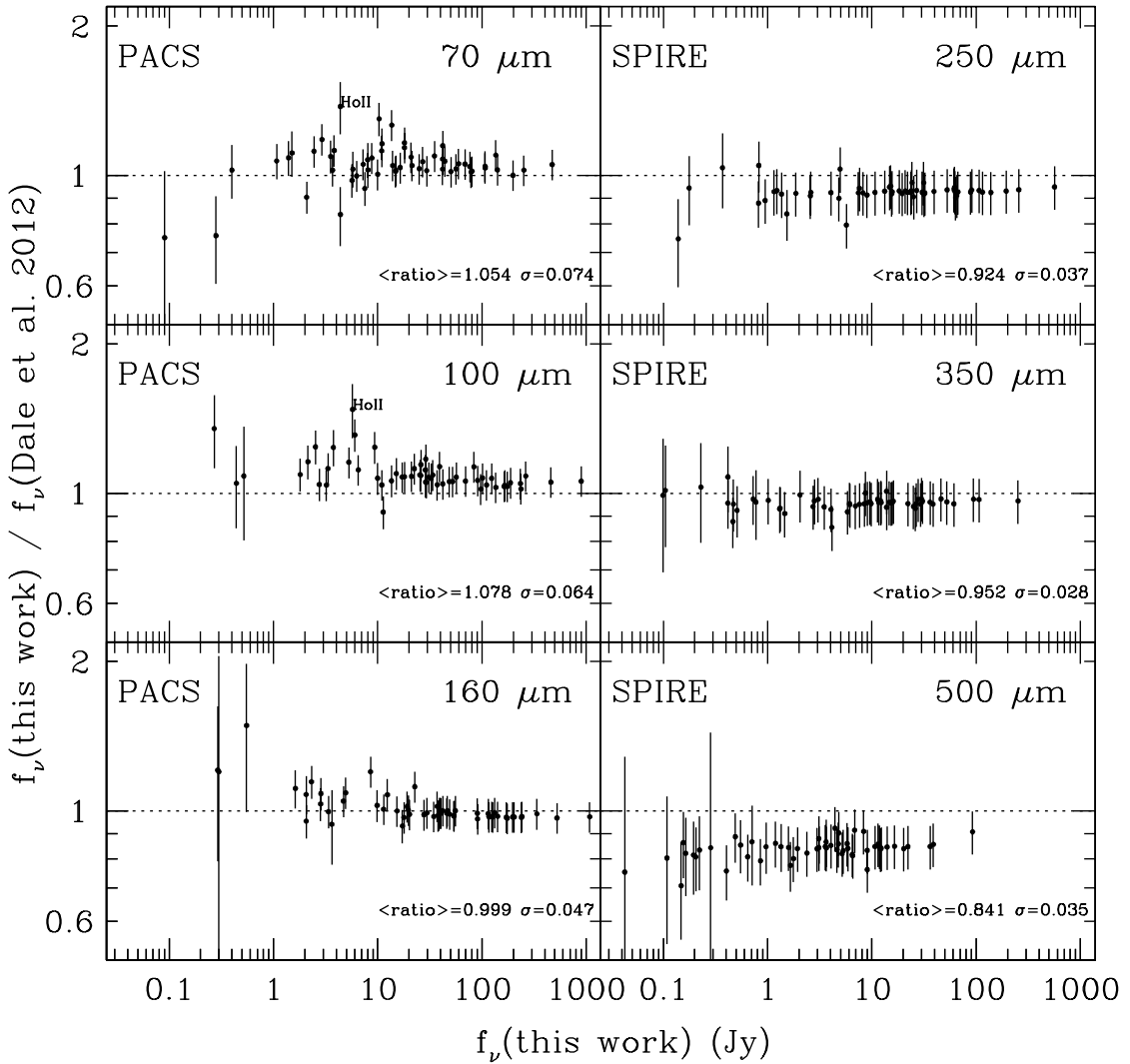


Figure 3. Comparison of updated global *Herschel* photometry with those presented in Dale et al. (2012). The error bars are relatively constant since they are primarily dominated by systematics for the brighter sources.

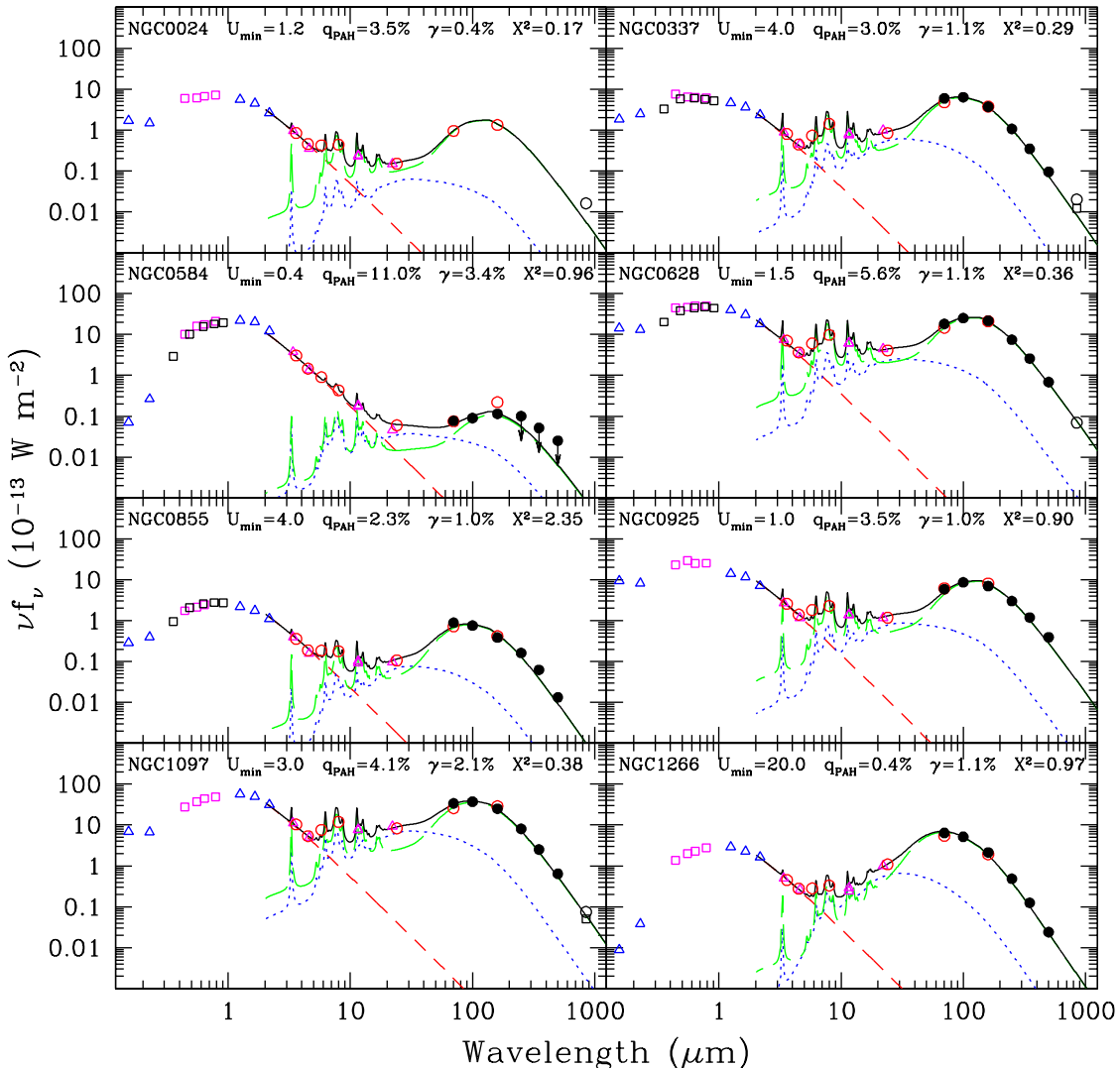


Figure 4. Globally-integrated infrared/sub-millimeter spectral energy distributions for all the galaxies in the KINGFISH/SINGS sample, sorted by Right Ascension. The following symbols are utilized: filled circles (*Herschel*), triangles (*GALEX*, *2MASS*, and *WISE*), open circles (*Spitzer* and *Planck*), squares (*BVRI*_C and *ugriz* and *SCUBA*). Arrows indicate 5 σ upper limits (and lower limits in the case of NGC 3034). The solid curve is the sum of a 5000 K stellar blackbody (short dashed) along with models of dust emission from PDRs (dotted; $U > U_{\min}$) and the diffuse interstellar medium (long dashed; $U = U_{\min}$). The fitted parameters from these [Draine & Li \(2007\)](#) 3.6–500 μm model fits are listed within each panel along with the reduced χ^2 (see § 4.2 for details). While the plotted data are corrected for Galactic extinction, the fluxes tabulated in Table 2 are not corrected. The uncertainties are smaller than the symbols plotted. There are no SED fits in cases where the far-infrared photometry provides only limits.

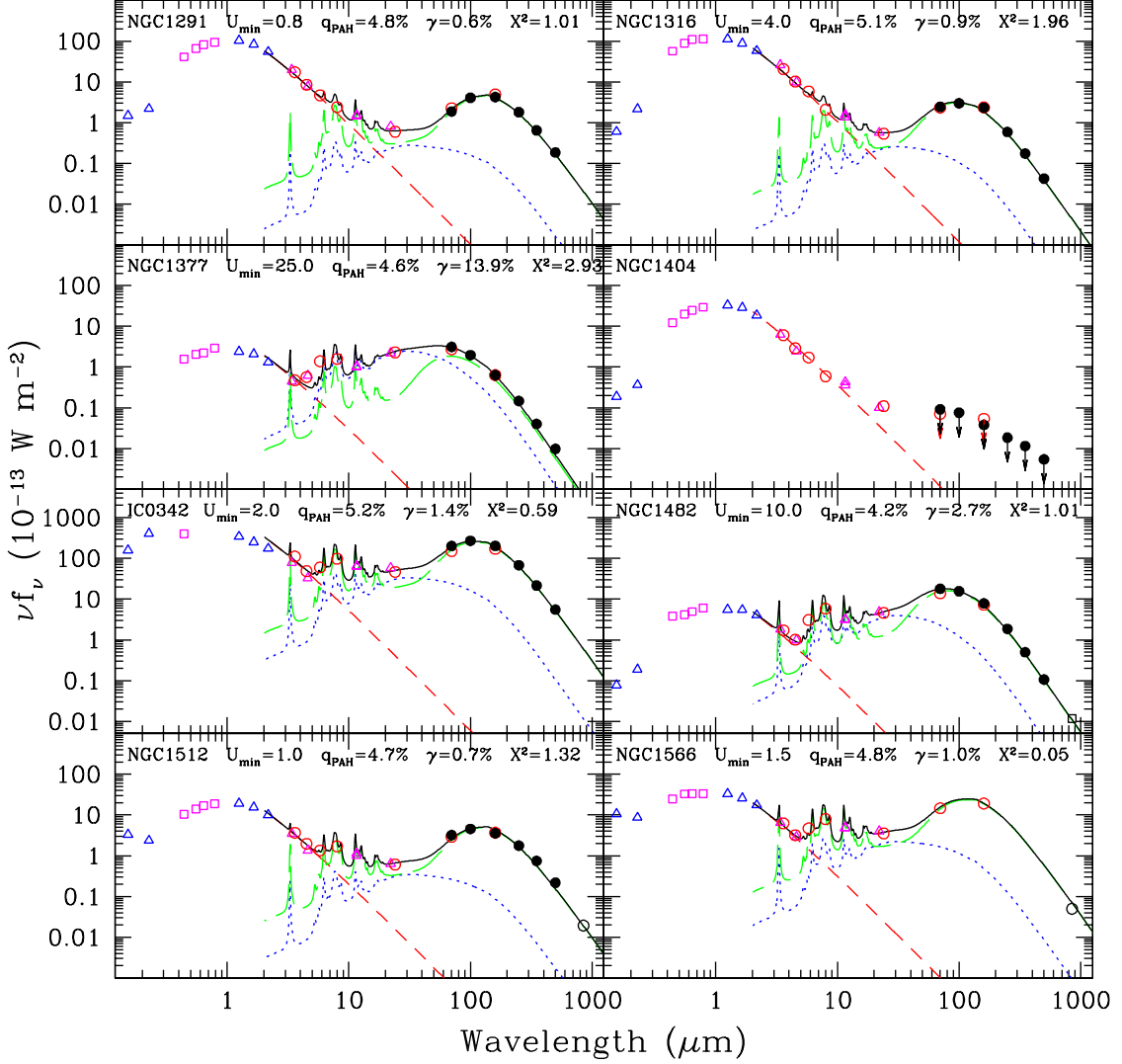


Figure 4. Globally-integrated infrared/sub-millimeter spectral energy distributions for the KINGFISH/SINGS sample (continued).

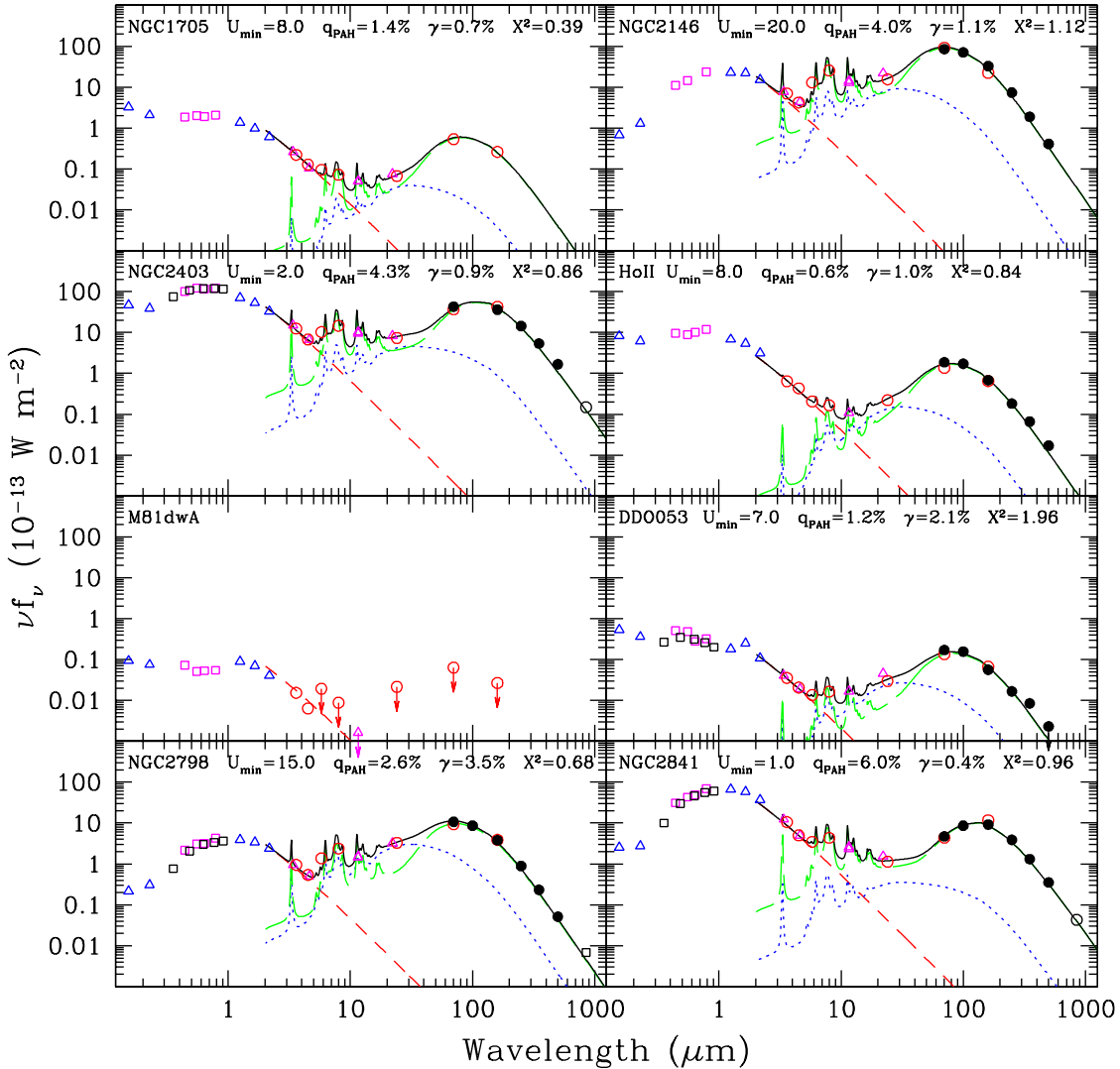


Figure 4. Globally-integrated infrared/sub-millimeter spectral energy distributions for the KINGFISH/SINGS sample (continued).

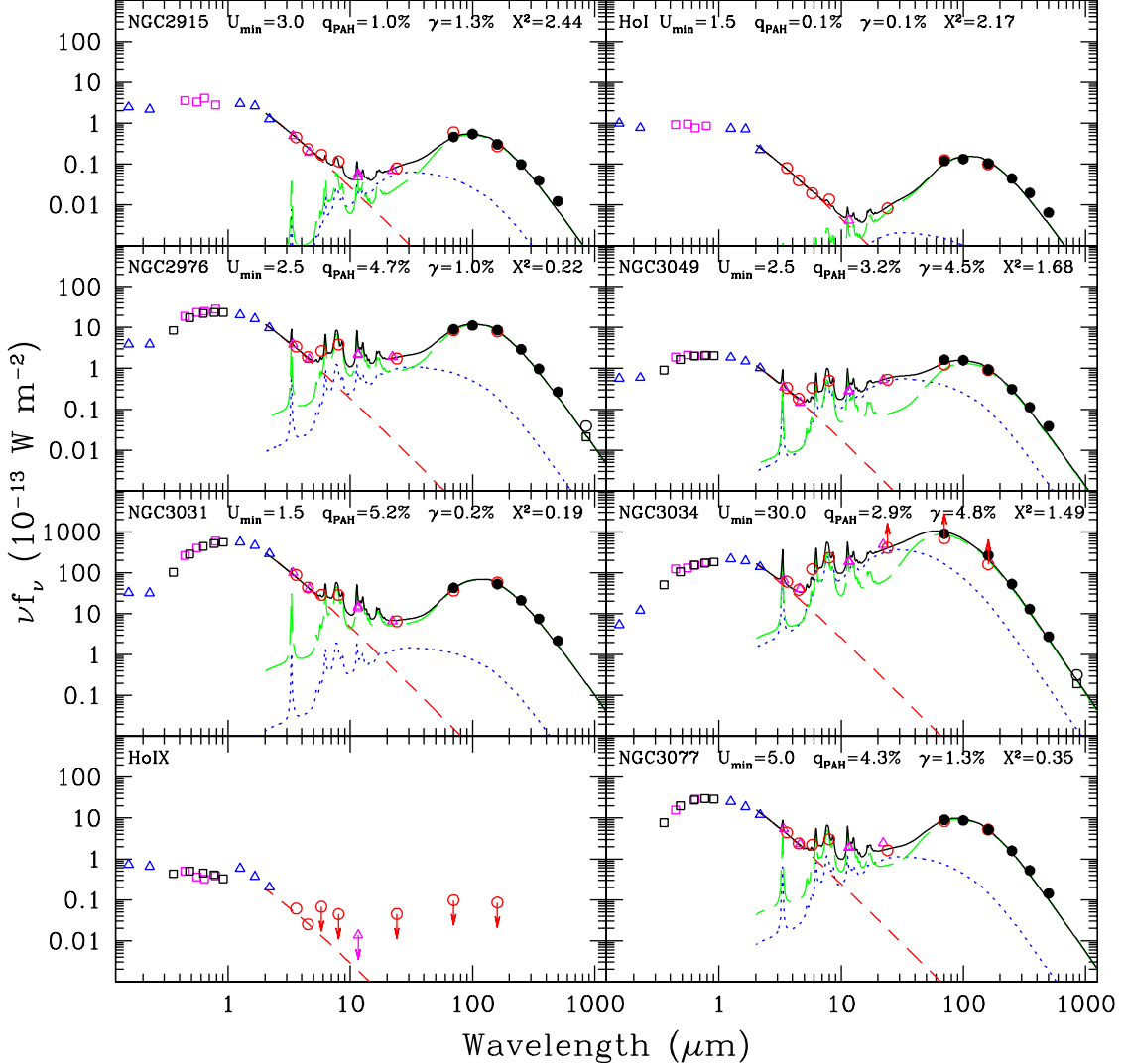


Figure 4. Globally-integrated infrared/sub-millimeter spectral energy distributions for the KINGFISH/SINGS sample (continued).

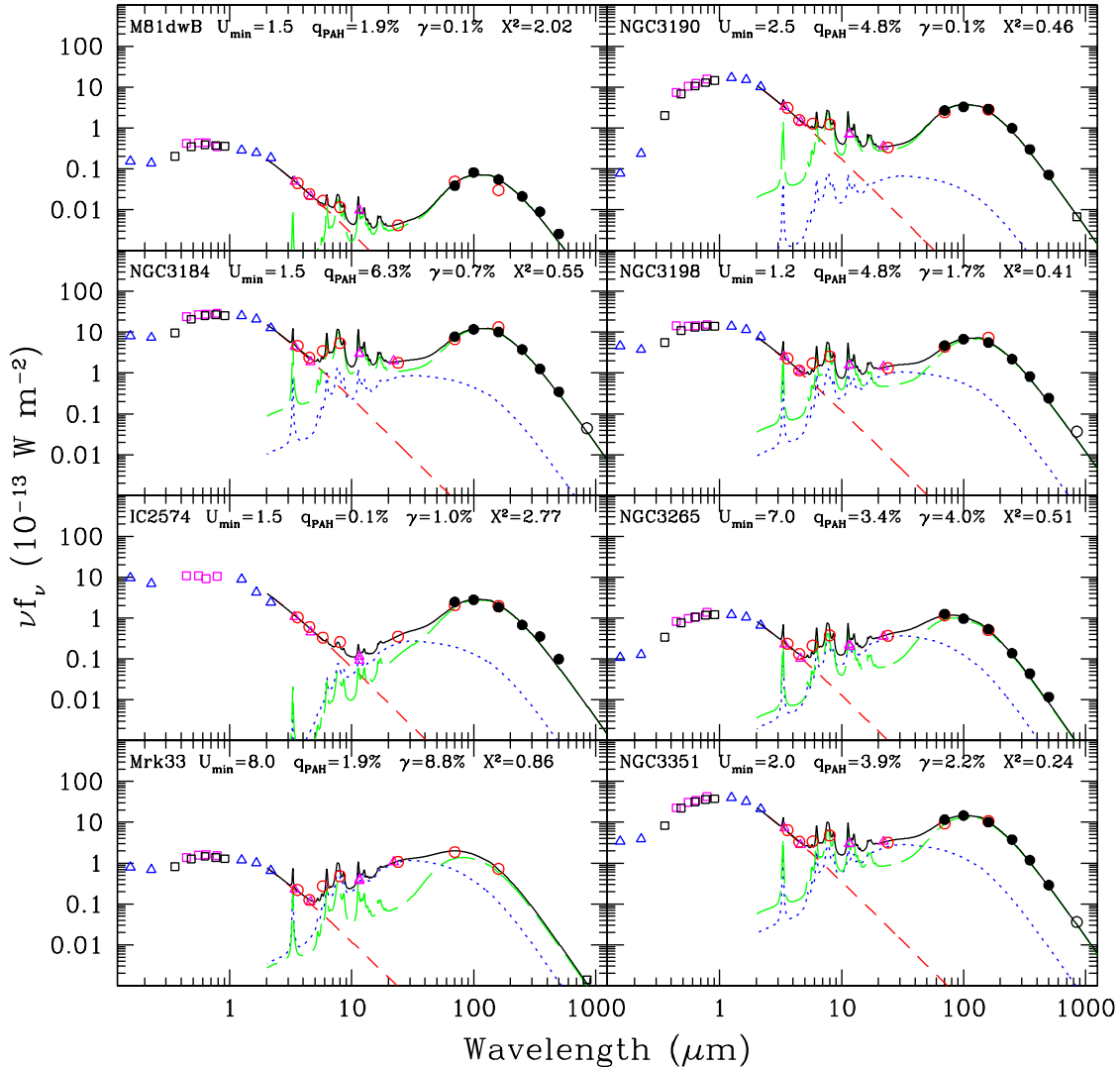


Figure 4. Globally-integrated infrared/sub-millimeter spectral energy distributions for the KINGFISH/SINGS sample (continued).

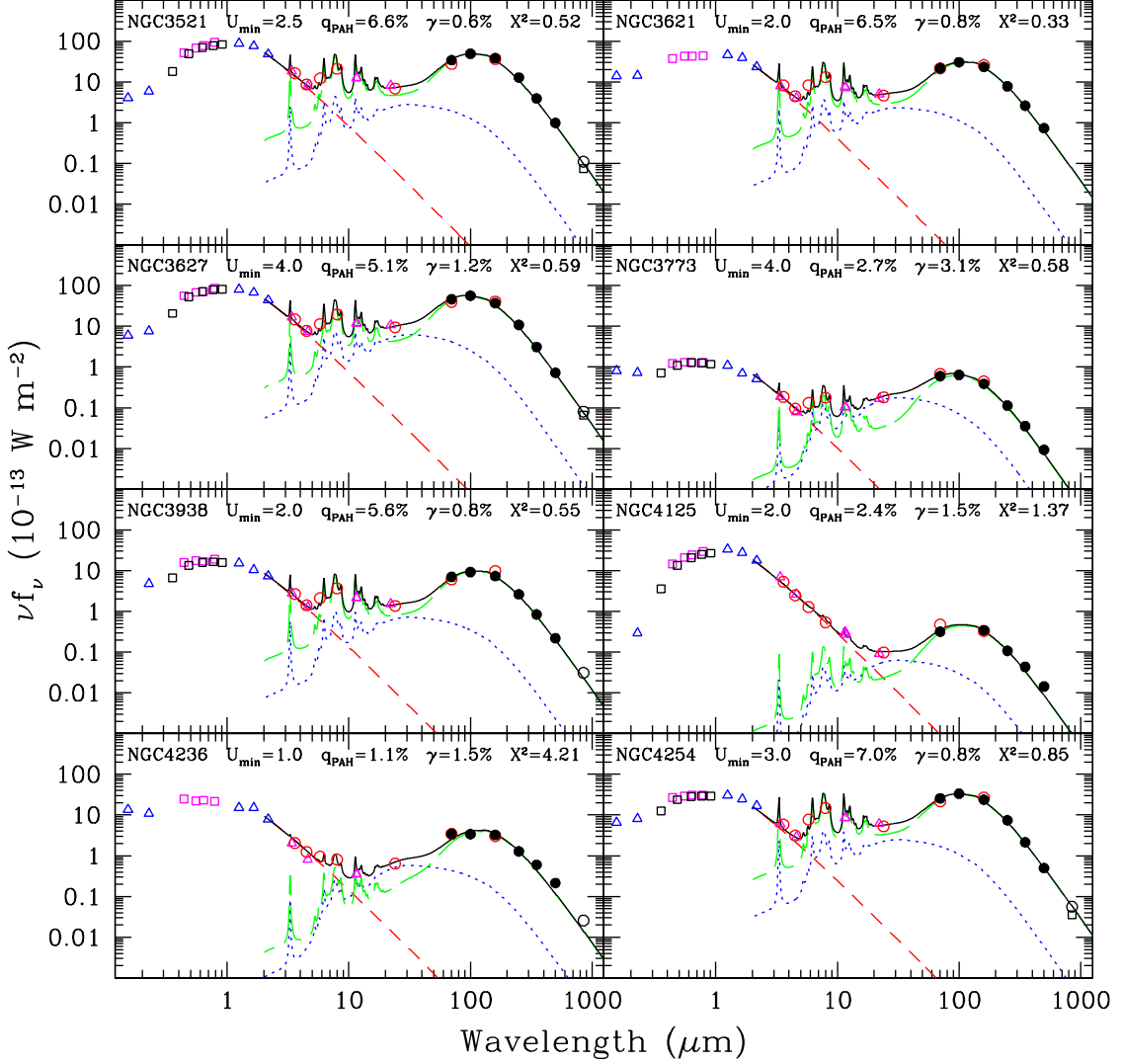


Figure 4. Globally-integrated infrared/sub-millimeter spectral energy distributions for the KINGFISH/SINGS sample (continued).

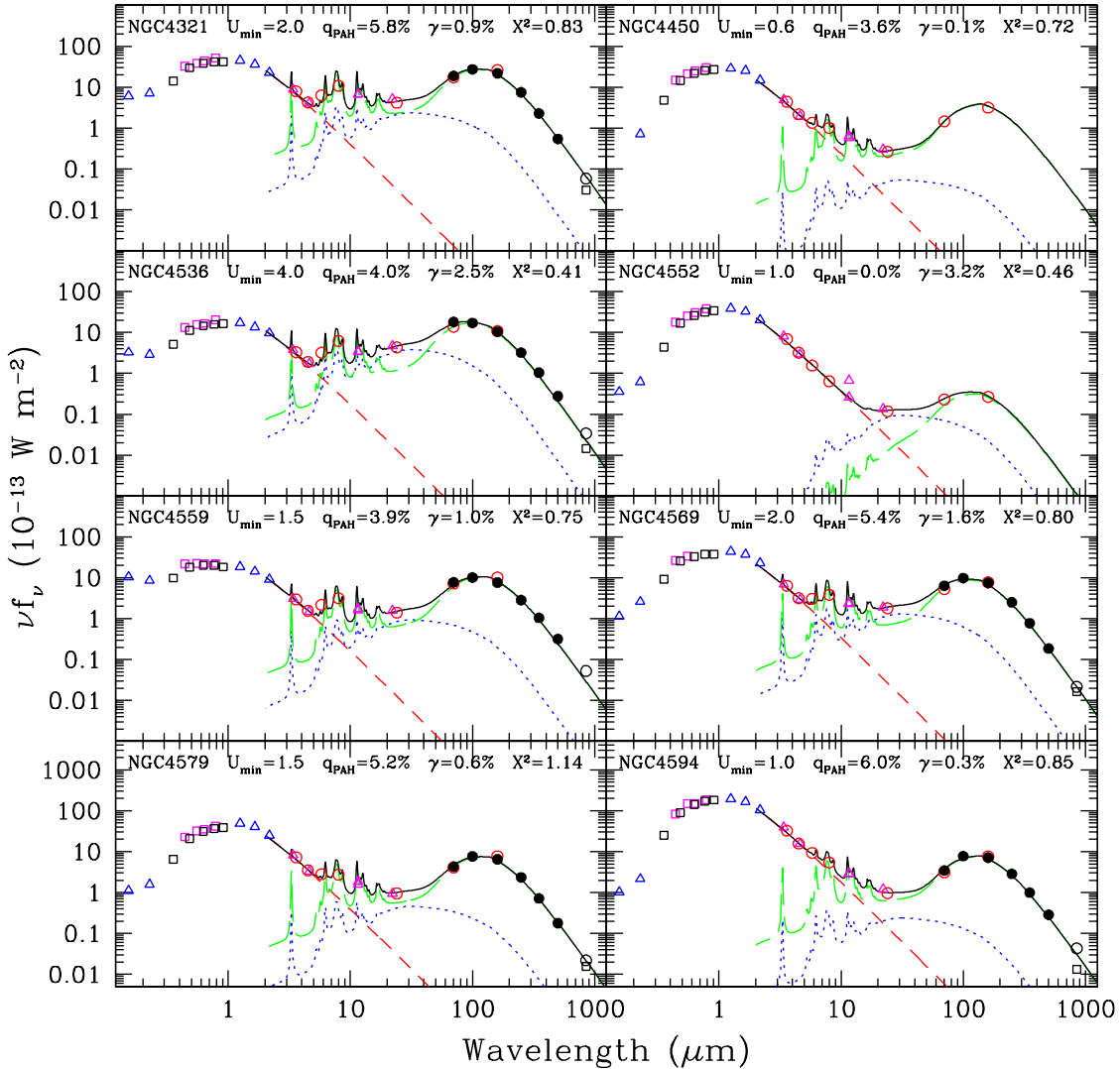


Figure 4. Globally-integrated infrared/sub-millimeter spectral energy distributions for the KINGFISH/SINGS sample (continued).

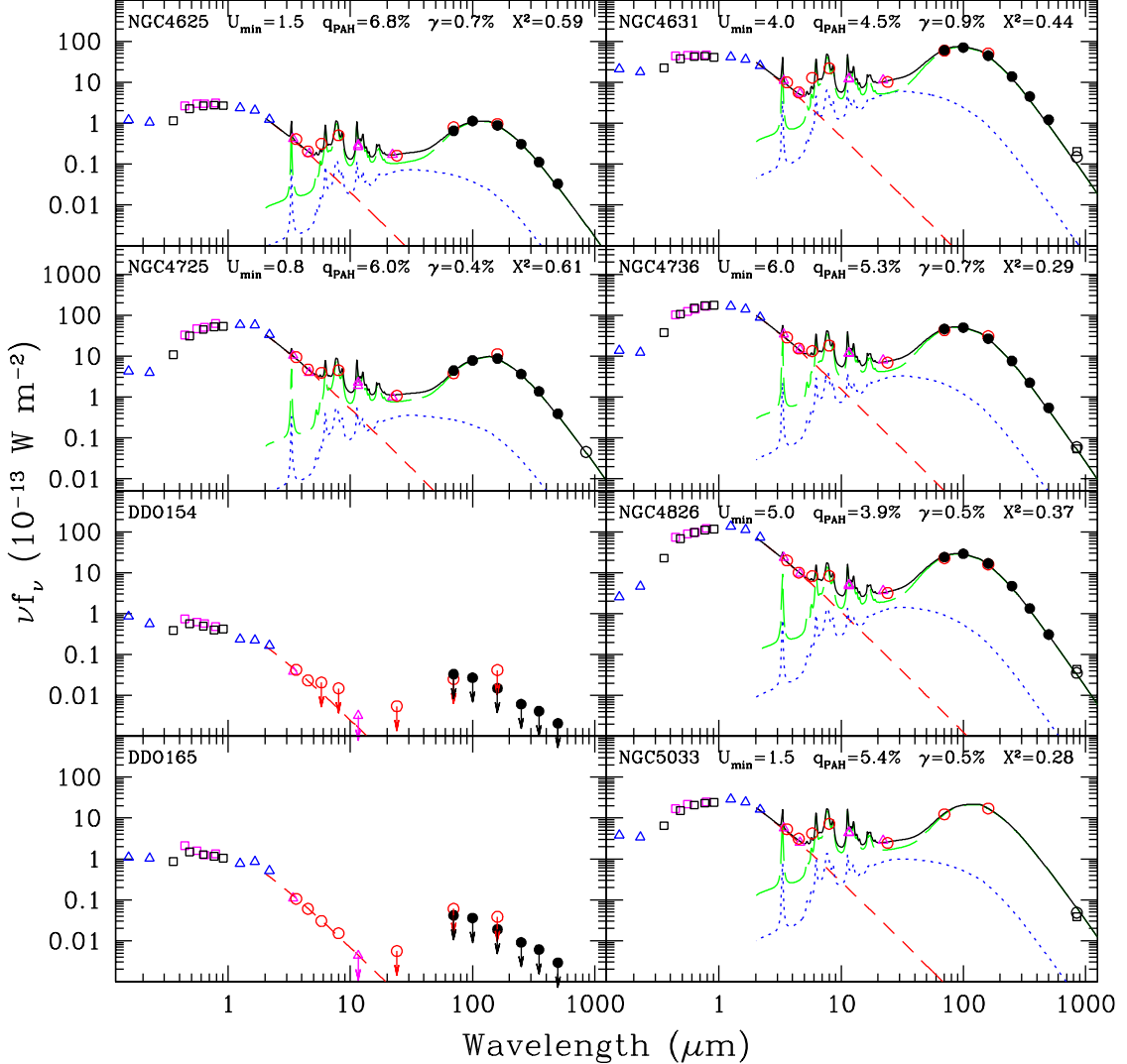


Figure 4. Globally-integrated infrared/sub-millimeter spectral energy distributions for the KINGFISH/SINGS sample (continued).

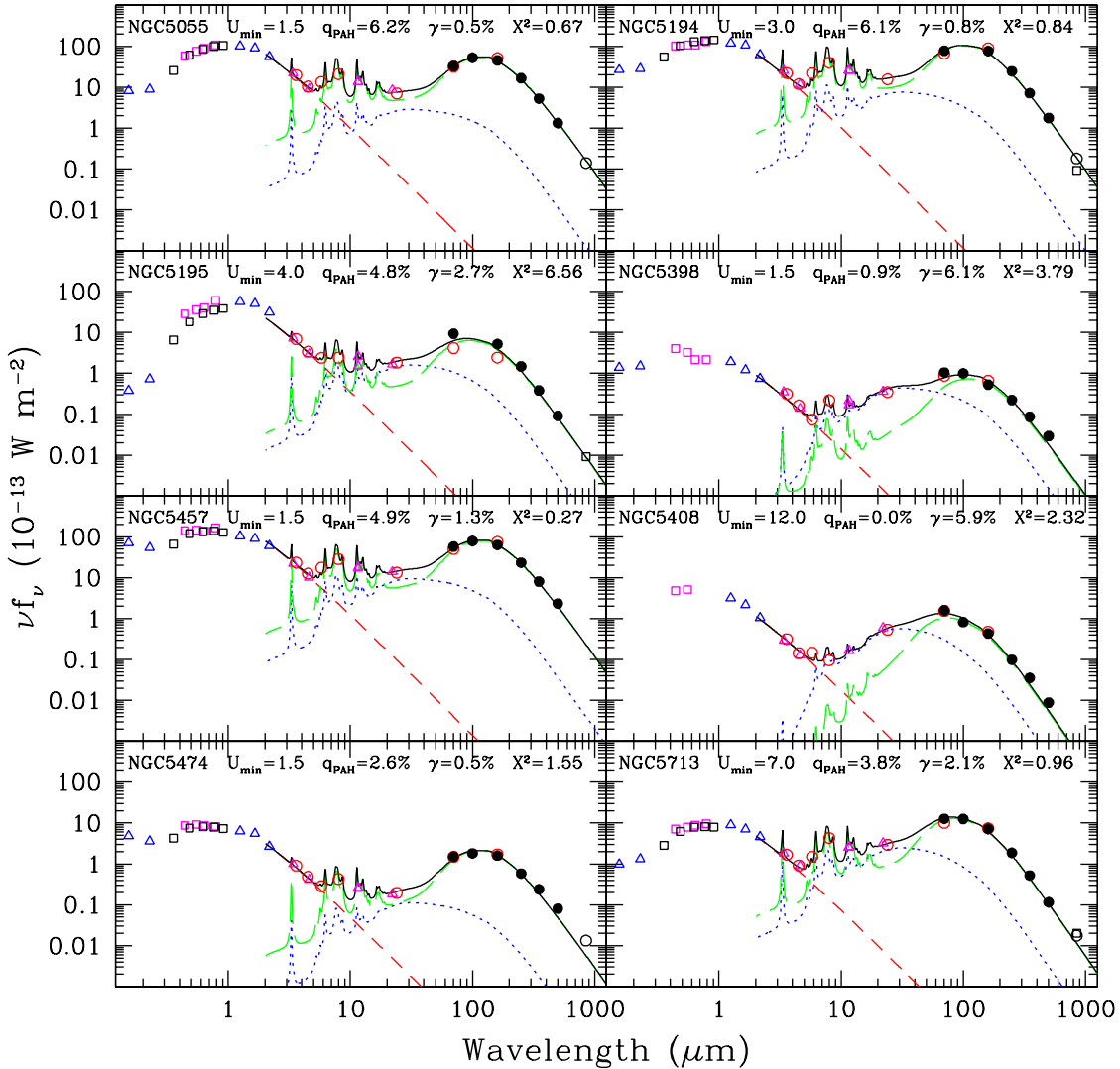


Figure 4. Globally-integrated infrared/sub-millimeter spectral energy distributions for the KINGFISH/SINGS sample (continued).

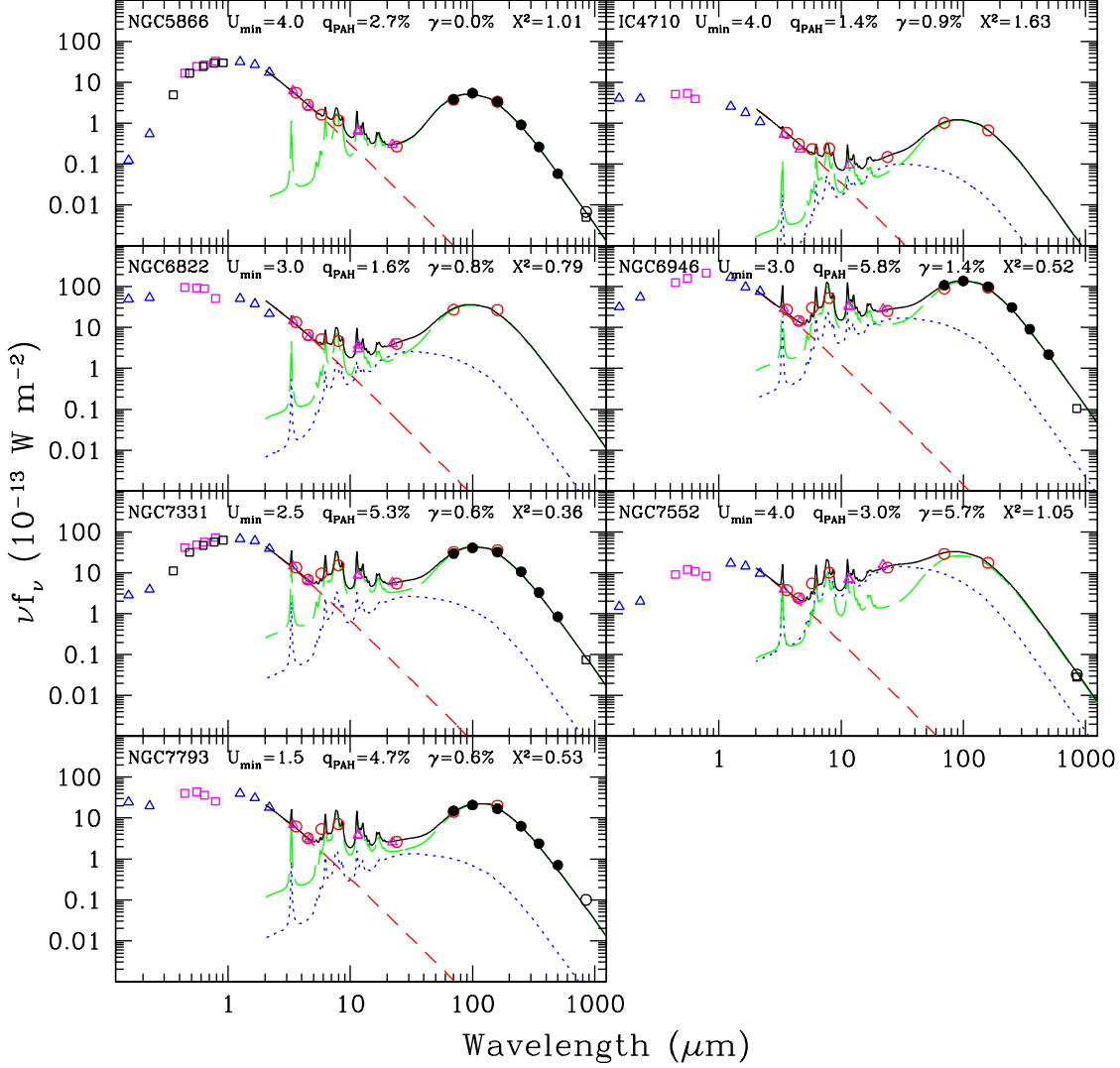


Figure 4. Globally-integrated infrared/sub-millimeter spectral energy distributions for the KINGFISH/SINGS sample (continued).

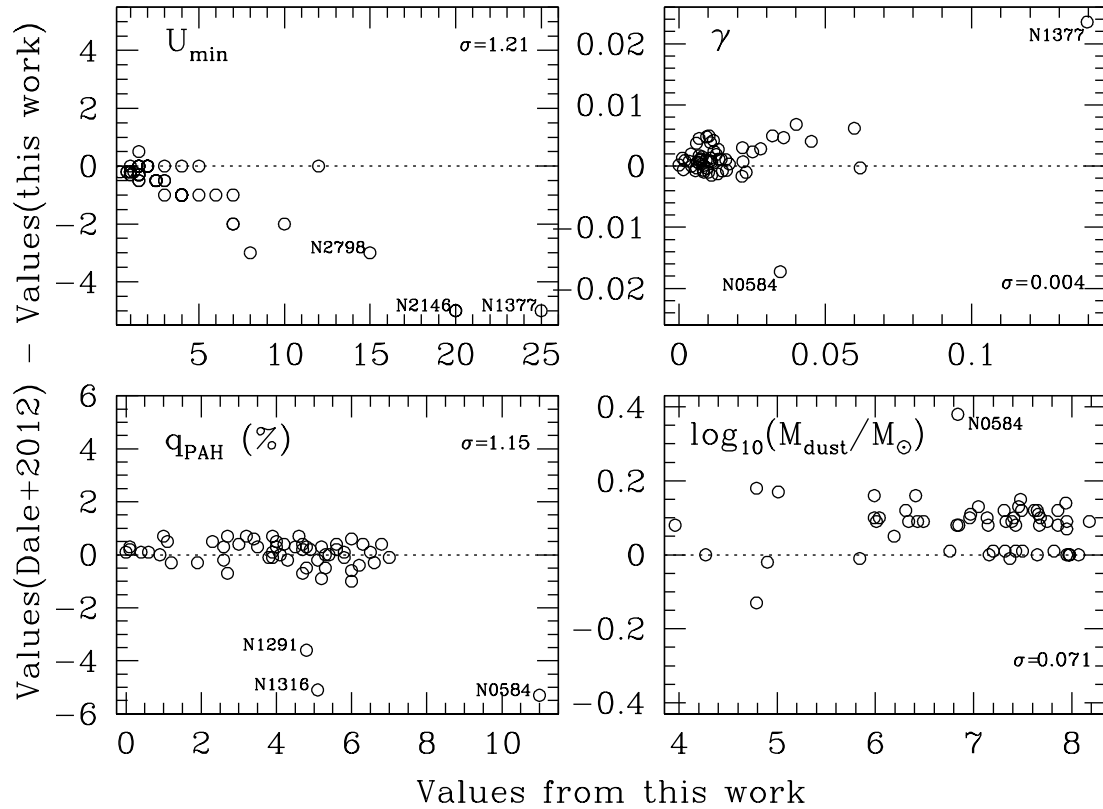


Figure 5. Comparison of DL07 output fit parameters from Dale et al. (2012) with those measured here. The dispersions in the ordinate (y-axis) values are inset.

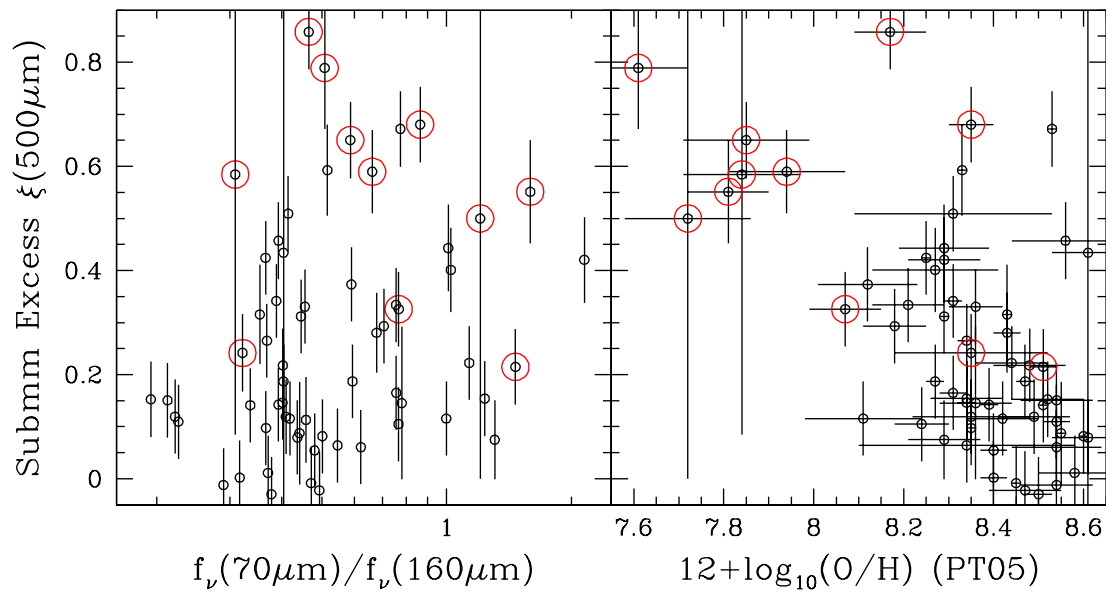


Figure 6. The submillimeter excess parameter $\xi(500\mu\text{m})$ (see Equation 6) as a function of far-infrared color and characteristic oxygen abundance as derived from [Moustakas et al. \(2010\)](#). Red circles indicate irregular galaxies ($T = \text{Sm, Im, or I0}$).

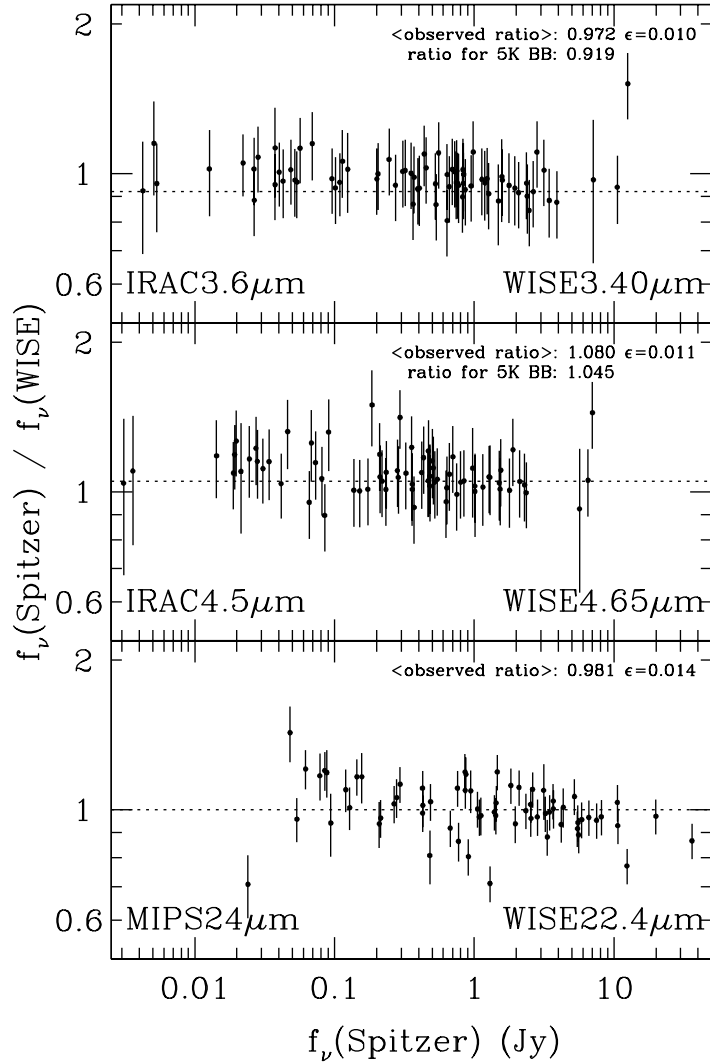


Figure 7. Comparison of *Spitzer*- and aperture-based global photometry with total WISE photometry. The dotted lines for the top two panels indicate the expected flux density ratios after convolving a 5000 K blackbody with the respective filter bandpass profiles. The average ratio and its uncertainty (σ/\sqrt{N}) are inset.